
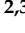




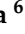
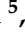





Article

Nature of Scapolite Color: Ab Initio Calculations, Spectroscopy, and Structural Study

Roman Shendrik ^{1,2,*}, Nikita V. Chukanov ^{2,3}, Alexander Bogdanov ¹, Alexandra Myasnikova ¹,
Elizaveta Pankrushina ⁴, Anatoly A. Zolotarev ⁵, Anastasiia Babkina ⁶, Ekaterina Popova ⁵, Marina F. Vigasina ²,
Sergey M. Aksenov ⁷, Grigoriy Ilyin ⁷ and Igor V. Pekov ^{2,*}

- ¹ Vinogradov Institute of Geochemistry, Siberian Branch of Russian Academy of Science, Irkutsk 664033, Russia; alex.bogdanov2012@gmail.com (A.B.); sasham@igc.irk.ru (A.M.)
 - ² Faculty of Geology, Moscow State University, Moscow 119991, Russia; chukanov@icp.ac.ru (N.V.C.); vigasina55@mail.ru (M.F.V.)
 - ³ Federal Research Center of Problems of Chemical Physics and Medicinal Chemistry, Russian Academy of Sciences, Chernogolovka 142432, Russia
 - ⁴ Zavaritsky Institute of Geology and Geochemistry, Ural Branch of the Russian Academy of Sciences, Ekaterinburg 620110, Russia; lizaveta.94@list.ru
 - ⁵ Institute of Earth Sciences, Saint-Petersburg State University, Saint-Petersburg 199034, Russia; a.a.zolotarev@spbu.ru (A.A.Z.); popovaekaterina@gmail.com (E.P.)
 - ⁶ Research Center of Optical Materials Science, ITMO University, Saint-Petersburg 197101, Russia; babkina.anastasya@bk.ru
 - ⁷ Laboratory of Arctic Mineralogy and Material Sciences, Kola Science Centre, Russian Academy of Sciences, Apatity 184200, Russia; aks.crys@gmail.com (S.M.A.); grinart7@gmail.com (G.I.)
- * Correspondence: r.shendrik@gmail.com (R.S.); igorpekov@mail.ru (I.V.P.)



Citation: Shendrik, R.; Chukanov, N.V.; Bogdanov, A.; Myasnikova, A.; Pankrushina, E.; Zolotarev, A.A.; Babkina, A.; Popova, E.; Vigasina, M.F.; Aksenov, S.M.; et al. Nature of Scapolite Color: Ab Initio Calculations, Spectroscopy, and Structural Study. *Minerals* **2024**, *14*, 937. <https://doi.org/10.3390/min14090937>

Academic Editors: Lluís Casas, Milen Kadiyski and Vladislav Kostov-Kytin

Received: 18 July 2024

Revised: 25 August 2024

Accepted: 11 September 2024

Published: 13 September 2024



Copyright: © 2024 by the authors. Licensee MDPI, Basel, Switzerland. This article is an open access article distributed under the terms and conditions of the Creative Commons Attribution (CC BY) license (<https://creativecommons.org/licenses/by/4.0/>).

Abstract: The article describes the results of a comprehensive study of the extra-framework components of scapolites using quantum–chemical calculations, electronic and vibrational spectroscopy, and single-crystal X-ray diffraction and crystal structure refinement. The ab initio calculations were performed using an embedded-cluster approach of extra-framework components in various cation surroundings. As a result, through comparing the experimental and ab initio calculation results, the energies of the electronic and vibrational transitions of various extra-framework components (CO_3^{2-} , $\text{CO}_3^{\cdot-}$, S_3^- , S_2^- —as well as the role of these components in the process of the lowering of the symmetry—were determined for scapolites belonging to the marialite–meionite solid–solution series. The nature of the various colors of the scapolites has also been established. Colors from purple to blue are a result of the presence of radiation-induced pairs of defects: carbonate radical anions ($\text{CO}_3^{\cdot-}$) and F-centers. However, polysulfide S_3^- radical anions are found in some violet scapolites.

Keywords: scapolite; marialite; meionite; ab initio calculations; polysulfide radical anion; carbonate radical anion; F-centers

1. Introduction

Scapolite-group minerals (scapolites) are tetragonal tectosilicates with aluminosilicate frameworks ($\text{Al}_{6-3}\text{Si}_{6-9}\text{O}_{24}$) that host $[(\text{Ca},\text{Na})_4(\text{CO}_3, \text{Cl}, \text{SO}_4, \text{Cl})]$ cation–anion clusters. They form a solid–solution system in which marialite, $\text{Na}_4(\text{Al}_3\text{Si}_9\text{O}_{24})\text{Cl}$, meionite, $\text{Ca}_4(\text{Al}_6\text{Si}_6\text{O}_{24})(\text{CO}_3)$, and silvialite, $\text{Ca}_4(\text{Al}_6\text{Si}_6\text{O}_{24})(\text{SO}_4)$, are the end-members belonging to the space group $I4/m$. Intermediate members of this solid–solution system may have a lower symmetry (as a rule, space group $P4_2/n$; rarely $P4$ or $P4/m$) [1–9].

In the crystal structures of scapolites, Si and Al are partly ordered. Despite the fact that Al–O–Al fragments tend to be unfavorable in aluminosilicate frameworks, it has been speculated that the highly charged $[\text{Ca}_4(\text{CO}_3)]^{6+}$ clusters may stabilize such local situations [1]. The most common subordinate components in scapolites are K^+ , Fe^{3+} , and H^+ ; some

other elements (Mg, Sr, F, etc.) occur in minor amounts [10]. In S-poor scapolites containing a meionite component comprising more than 25%, the main replacement schemes are $\text{Na}_3\text{Si}_2\text{Cl} \rightarrow \text{Ca}_3\text{Al}_2(\text{CO}_3)$ and $\text{NaSi} \rightarrow \text{CaAl}$ in solid–solution series with ordered and disordered extra-framework $[(\text{Ca},\text{Na})_4(\text{CO}_3,\text{Cl})]$ clusters, respectively [1].

The minor deficiency of extra-framework metal cations as compared to the ideal value of four atoms per formula unit (apfu) and the presence of hydrogen are rather common for scapolites [10]. However, the role of hydrogen in these minerals has remained insufficiently studied for a long time.

Scapolites are important components of many different kinds of metamorphic and metasomatic rocks. Geological and geochemical studies of marialites were recently performed, as presented in [11]. Some varieties of these minerals may serve as indicators of physical and chemical conditions of ore formation. Gem-quality marialite (colorless, yellow, violet, and lilac) is known to be found in some alkaline metasomatites that are hosted by marbles [12–15]. Despite the long-term study of scapolites, the nature of their color remains unclear. It has been established that colored marialites and blue meionites often become discolored when they are heated above 400–450 °C [12,16–18]. On the other hand, their color is restored by X-ray irradiation [12,16,18,19], as well as by short-wave ultraviolet irradiation; in our opinion, it is not entirely correctly to call this photochromism [14,20–22]. It is obvious that the color of scapolites is associated with radiation-induced defects. However, the nature of these defects remains controversial. In some studies [12], it is assumed that the color is associated with SO_2^- , SO_3^- radical anions, and Mn^{3+} [23]; meanwhile, other studies, such as [19], purport that it can be attributed to O^- radical anions. Additionally, the potential role of F-centers in the blue coloration of scapolites was discussed in [22]. In another work [16], it was assumed that carbonate radical anions act as blue chromophores. Later, this was confirmed in a subsequent study [18], and the exciton mechanism for the occurrence of such defects was established.

The luminescence of scapolites has also been studied in a number of studies. The characteristic orange luminescence is associated with S_2^- centers [24–26]. It has also been established that luminescence of Fe^{3+} can be observed in the red spectral region [16], and the luminescence of Mn^{2+} can be observed in the green region of the spectrum [18].

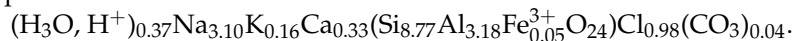
In this work, the extra-framework components in scapolites of different origins, including their color and luminescence centers, as well as the roles of hydrogen in these minerals, were studied. The studies were conducted using a set of methods including infrared (IR), Raman, electron spin resonance (ESR), UV–Vis–near-IR absorption and photoluminescence spectroscopy, and electron microprobe analysis. Impurity centers were identified based on the comparison of the experimental data with the results of ab initio quantum–chemical calculations.

2. Materials and Methods

2.1. Samples

The studied samples are listed below. Data on their chemical compositions, based on electron microprobe analyses, are given in Table 1. The contents of H_3O^+ and $(\text{CO}_3)^{2-}$ in the empirical formulae were calculated based on the charge-balance requirement under the condition that the number of extra-framework cations per formula unit (pfu) is equal to 4. The presence of H_3O^+ and $(\text{CO}_3)^{2-}$ in the studied samples was confirmed by IR and Raman spectroscopy (see below). Samples 3614, 2386, 250, 1366, and 418 are from the collection of one of the co-authors (N.V.C.). Sample 54,413 is deposited in the Fersman Mineralogical Museum of the Russian Academy of Sciences, Moscow. Sample 11/446 is from the Sidorov Mineralogical Museum of the Irkutsk National Research Technical University. Sample S-22 is from the collection of one of the co-authors (A.A.Z.).

Sample 3614 (Figure 1a) is lilac prismatic crystal of marialite from the Kukurt gem scapolite deposit, Muzkol metamorphic complex, Eastern Pamirs, Tajikistan. The mineral originates from a cavity in hydrothermal vein mainly composed of marialite and albite with subordinate amounts of rutile, titanite, and ilmenite [12]. The empirical formula of Sample 3614 is:



Sample 2386 (Figure 1b) is a transparent, gem-quality yellow Ca-bearing marialite from the Kukurt deposit. The empirical formula of this sample is:

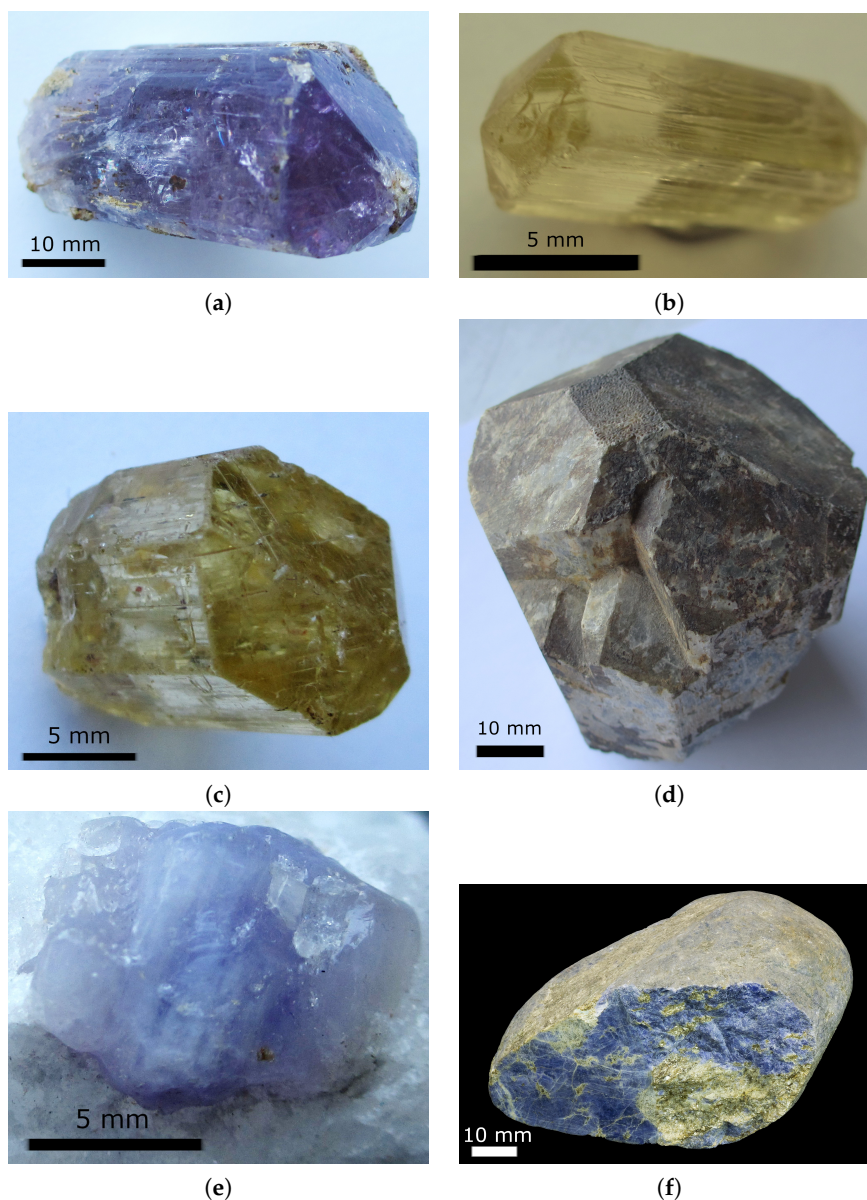
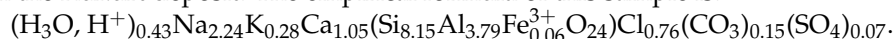
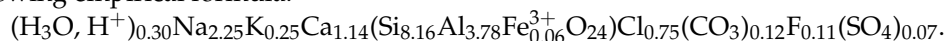
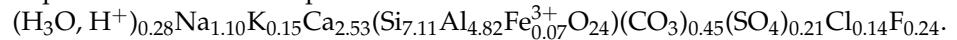


Figure 1. Samples 3614 (a), 2386 (b), 250 (c), 1366 (d), 418 (e), and 11/446 (f). The field of view (FOV) widths are 4.1, 1.3, 2.1, 6.3, 1.2, and 9.5 cm, respectively.

Sample 250 (Figure 1c) originates from the Morogoro marble occurrence, Uluguru Mts., Tanzania. It forms a transparent yellow prismatic crystal as a result of association with feldspar and corundum. The chemical composition of Sample 250 corresponds to the following empirical formula:

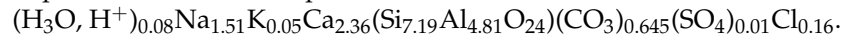


Sample 1366 (Figure 1d) is a pale-green prismatic crystal of SO_4^- and F-bearing meionite from the Kanku skarn phlogopite deposit, Aldan Region, Sakha Republic, Russia. The associated minerals are calcite, F-rich phlogopite, fluorapatite, diopside, and spinel. The empirical formula of Sample 1366 is as follows:

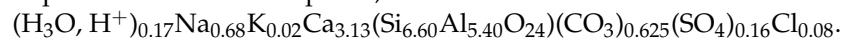


Sample 418 (Figure 1e) is violet–blue meionite (“glaucolite”) from the Slyudyanka river valley, Slyudyanka district, Baikal Lake Region, Siberia, Russia.

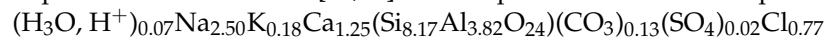
Sample 54,413 studied by us earlier [27] is a violet–blue “glaucolite” similar to Sample 418. It forms a coarse-grained nest (8 cm across), rimmed by phlogopite, in calcite marble. The empirical formula of Sample 54413 is as follows:



Sample 11/446 (Figure 1f) was partly studied earlier [18]. It occurs as an aggregate of violet–blue translucent individuals up to 5×3 mm in association with yellow mica. The empirical formula of Sample 54,413 is as follows:



Sample S-22 originates from the Turakuloma range, Eastern Pamirs, Tajikistan. A similar sample has been studied in [12,23]. The empirical formula of Sample S-22 is as follows:



Sample Sh-1 is marialite from the Kukurt deposit. It was chosen for single-crystal X-ray structure analysis after testing the symmetry of 10 marialite samples from this locality. The testing procedure showed that samples with Ca contents below 0.9 apfu belong to the space group $I4/m$, whereas all samples with higher Ca contents have lower symmetry (space group $P4_2/n$). The empirical formula of Sample Sh-1—derived based on electron microprobe analyses with a JXA-733 device, produced by JEOL (Tokyo, Japan), equipped with an EDS spectrometer and an INCA Energy 350 analyzer (Oxford, UK)—is as follows:



Table 1. Chemical compositions of the scapolite samples studied in this work.

Sample Number	3614	2386	250	1366	11/446 ¹	S-22 ²
Component	Content (wt.%)					
Na ₂ O	11.26	7.99	7.96	3.78	2.31	8.67
K ₂ O	0.90	1.53	1.33	0.75	0.12	0.95
CaO	2.14	6.67	7.31	15.70	19.38	7.82
Al ₂ O ₃	19.04	22.27	21.99	27.13	30.30	21.75
Fe ₂ O ₃	0.48	0.55	0.53	0.65	bdl	0.04
SiO ₂	61.83	56.41	55.93	47.22	43.80	54.91
SO ₃	bdl	0.63	0.66	1.88	1.38	0.14
F	bdl	bdl	0.23	0.51	bdl	bdl
Cl	4.06	3.10	3.03	0.54	0.30	3.05
-O≡Cl,F	−0.92	−0.71	−0.78	−0.34	−0.08	−0.69
Total	98.79	98.44	98.19	97.82	97.51	96.64
Formula coefficients calculated on Si + Al + Fe = 12 apfu						
Na	3.10	2.24	2.25	1.10	0.68	2.50
K	0.16	0.28	0.25	0.15	0.02	0.18
Ca	0.33	1.05	1.14	2.53	3.13	1.25
Al	3.18	3.79	3.78	4.82	5.40	3.82
Fe	0.05	0.06	0.06	0.07	-	-
Si	8.77	8.15	8.16	7.11	6.60	8.17
S	-	0.07	0.07	0.21	0.16	0.02
F	-	-	0.11	0.24	-	-
Cl	0.98	0.76	0.75	0.14	0.08	0.77

Notes: ¹ [18]. bdl means “below detection limit”. ² [12].

2.2. Analytical Methods

In order to obtain infrared (IR) absorption spectra, powdered samples were mixed with anhydrous KBr, pelletized, and analyzed using an ALPHA FTIR spectrometer (Bruker Optics, Karlsruhe, Germany) at a resolution of 4 cm^{-1} in Federal Research Center of Problems of Chemical Physics and Medicinal Chemistry, Russian Academy of Sciences. A total of 16 scans were collected for each spectrum. The IR spectrum of an analogous pellet of pure KBr was used as a reference.

The Raman spectra of the natural samples were obtained for randomly oriented grains using an EnSpectr R532 spectrometer based on an OLYMPUS CX 41 microscope (Enhanced Spectrometry, San Jose, CA, USA) coupled with a diode laser ($\lambda = 532\text{ nm}$) at room temperature in Faculty of Geology, Moscow State University. The spectra were recorded in a range from 100 to 4000 cm^{-1} with a diffraction grating (1800 gr mm^{-1}) and spectral resolution about 6 cm^{-1} . The output power of the laser beam was in the range from 5 to 13 mW . The diameter of the focal spot on the sample was $5\text{--}10\text{ }\mu\text{m}$. The back-scattered Raman signal was collected with a $40\times$ objective. The signal acquisition time for a single scan of the spectral range was 1 s , and the signal was averaged over 50 scans. Crystalline silicon was used as a standard. Raman spectrum of Sample S-22 was registered using a Horiba LabRam HR800 Evolution instrument equipped with an Olympus BX-FM confocal microscope in Zavaritsky Institute of Geology and Geochemistry, Ural Branch of the Russian Academy of Sciences. An argon laser with a radiation wavelength of 488 nm and a laser power of 5 mW was employed. A $50\times$ objective lens with a numerical aperture of 0.7 was used. The acquisition time was 100 s with 2 accumulations per spectral segment. The spectra were recorded using a diffraction grating of 1800 gr/mm and an electrically cooled charge-coupled device detector.

The EDS-mode electron microprobe analyses were carried out on an analytical suite including a digital scanning electron microscope (Tescan VEGA-II XMU) equipped with an energy-dispersive spectrometer (EDS) (INCA Energy 450) with a semiconducting Si(Li) detector (Link INCA Energy) and a wave-dispersive spectrometer (WDS) (Oxford INCA Wave 700, produced by Tescan Orsay Hld., Brno, Czech Republic in Faculty of Geology, Moscow State University). The analyses were performed at an accelerating voltage of 20 kV , with a current of $120\text{--}150\text{ pA}$ and a beam diameter of 120 nm . The diameter of the excitation zone was below $5\text{ }\mu\text{m}$. The following standards were used: CaF_2 for F, albite for Na, synthetic Al_2O_3 for Al, wollastonite for Ca, potassium feldspar for K, SiO_2 for Si, Fe metal for Fe, and FeS_2 for S. The contents of other elements with atomic numbers > 6 were below the detection limits.

The absorption spectra in the near-infrared, visible, and ultraviolet (NIR/Vis/UV) ranges were measured at room temperature using a Lambda 950 spectrophotometer (Perkin-Elmer, Shelton, CT, USA). The ESR spectra were measured with a RE-1306 X-band spectrometer (KBST, Smolensk, Russia) with a frequency of 9.3841 GHz at room temperature. The photoluminescence spectra were measured using an LS-55 spectrofluorimeter (Perkin-Elmer, Shelton, CT, USA) at room temperature. Photoluminescence excitation spectra were corrected for the varying intensities of excitation light. The spectroscopy experiments were performed in Vinogradov Institute of Geochemistry SB RAS.

The X-ray diffraction were collected at room temperature on a XtaLAB Synergy diffractometer with a graphite monochromatized MoK_α radiation source ($\lambda = 0.71073\text{ \AA}$) and a Hybrid Pixel Array detector in Laboratory of Arctic Mineralogy and Material Sciences, Kola Science Center, Russian Academy of Sciences. Unit cell parameters were determined and refined, and data were integrated and corrected for background, Lorentz, and polarization effects using the CrysAlis software, version 1.171 [28]. The tetragonal unit cell parameters were as follows: $a = 12.0457(3)\text{ \AA}$, $c = 7.5683(1)\text{ \AA}$; $V = 1098.15(4)\text{ \AA}^3$. A total of $14,211$ reflections within the sphere delimited by $\theta = 30.96^\circ$ were measured. Systematic absences violate the I -centering indicated the most likely space group was $P4_2/n$, which was finally chosen for the refinement. The crystal structural data, the experimental characteristics, and the results of the refinement of the structure of Sample Sh-1 are given

in Table S1. The crystal structure of Sample Sh-1 was determined and refined using the JANA2006 program [29] to the final R value of 3.1% using 1204 reflections with $I > 3\sigma(I)$ in the anisotropic approximation of atomic displacements. Because of the complex chemical composition, the cation distribution on the structural sites (Table S2) was proposed taking the site-scattering factors, inter-atomic distances, and ionic radii of the cations into account: at the first step, the number of electrons associated with the atoms at the site (e_{calc}) [30] was determined; at the second step, for each value of e_{calc} , the most suitable ratio between the atoms with the closest final refined amount of electrons (e_{ref}) was selected and the atoms' coordinates and ADPs were refined.

Table S2 lists the fractional atomic coordinates, occupancy, site symmetry, and equivalent isotropic atomic displacement parameters (U_{eq}). The selected inter-atomic distances are given in Table S3.

2.3. Computation Methods

The procedure of calculation was divided into two steps: the first step was geometry relaxation of scapolite unit cells containing studied complexes under periodic boundary conditions and the second step involved the calculation of electronic, optical, and vibrational properties with an embedded-cluster approach. The periodic boundary calculations for the F-center, carbonate, and polysulfide radical anions ($(\text{CO}_3)^{2-}$, F-center, S_2^- , S_3^-) were implemented in VASP simulation package [31]. The calculations were performed on an "Academician V.M. Matrosov" computational cluster [32]. The $(\text{CO}_3)^-$ was optimized with the use of the CP2K [33] software package. The PBEsol [34] functional was used in both codes as an approximation for the exchange-correlation term in the Hamiltonian. In VASP, the chosen cutoff energy for the plane wave basis set was 400 eV. In CP2K, we used standard DZVP-MOLOPT-PBE-GTH basis sets with GTH-PBE potentials. The atomic positions were optimized with 0.01 eV/Å stop-criteria for forces. The lattice vectors were fixed at their experimental values ($a = b = 12.060$ Å, $c = 7.587$ Å). The complexes were modeled within different $\text{Na}_{4-x}\text{Ca}_x$ environments for x ranging from 0 to 4. The charge compensation for Na-Ca replacement was preserved through Si-Al replacement.

The IR, Raman, ESR, and optical properties were calculated within the ORCA program package [35]. Structural information required for this step was taken from VASP/CP2K optimization results, and complexes were modeled using an embedded-cluster approach [36]. An example of embedded cluster is presented in Figure 2. The inner region I is the quantum cluster for which electron paramagnetic resonance, optical absorption, and vibrational properties are calculated. It contains the calculated species (F-center, $(\text{CO}_3)^{2-}$, $(\text{CO}_3)^-$, S_2^- , S_3^-) and the Na/Ca ions nearest to them in a total of four–eight atoms. The quantum cluster is surrounded by region II, where point charges with effective core potentials (ECP) are added. The ECP region is used to prevent charge leakage from the quantum cluster. The size of the ECP region is approximately 400 point charges. The ECP area is surrounded by a region of point charges, which is used to represent the electrostatic field of the crystal. The molecular orbitals within the quantum region were represented using Gaussian basis set def2-tzvp. The Stuttgart/Dresden (SDD) potentials were used within the ECP region. The point charges in the ECP and PC areas were as follows: -2 for O, -1 for Cl, $+1$ for Na, $+2$ for Ca, $+3$ for Al, $+4$ for Si, and $+4$ for C. For the polysulfide species, the point charges for S were selected in order to obtain -1 for the modeled species. The hybrid B3LYP [37] exchange-correlation functional was used. The optical properties were calculated using TDDFT method without Tamm–Danncoff approximation. For vibrational properties calculation, the positions of the Na/Ca ions were fixed and the partial hessian was calculated. The calculations were performed at 0 Pa pressure and 0 K temperature.

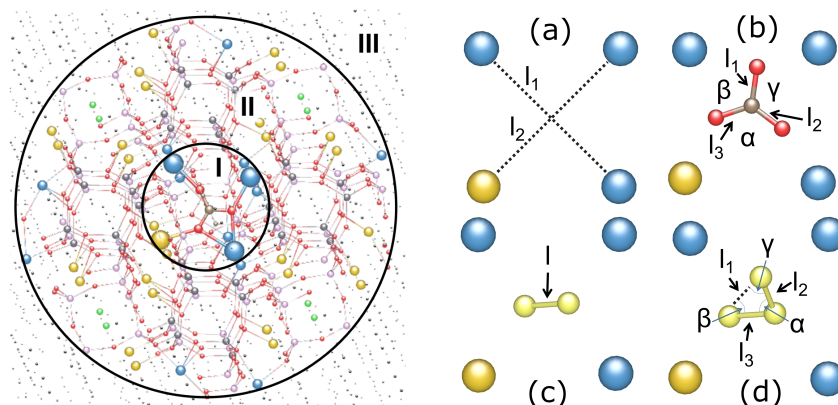


Figure 2. Example of embedded cluster (left side): region I is quantum cluster, II is ECP region, III—point charge region—and configuration of different extra-framework centers (right side): (a) F-center; (b) $(CO_3)^{2-}$; (c) S_2^{2-} ; (d) S_3^{2-} .

3. Results

3.1. Ab Initio Calculations

3.1.1. $(CO_3)^{2-}$ and $(CO_3)^{-}$ Groups

The $(CO_3)^{2-}$ group is the dominant extra-framework anion in meionite. It is usually surrounded by four Ca^{2+} cations. However, other options are also possible, which can generally be written as Na_xCa_{4-x} , where $x = 0-4$ [4]. In this case, charge compensation is achieved by varying the ratios of silicon–oxygen and aluminum–oxygen tetrahedra. The geometry of the $Na_xCa_{(4-x)}^{(8-x)+}(CO_3)^{2-}$ complex has been optimized for all possible Ca:(Na+Ca) ratios. The geometric parameters are given in Table 2.

Table 2. The geometry of the $(CO_3)^{2-}$ anion in various cation environments.

	α	β	γ	l_1	l_2	l_3
Na₄	123.2	118.7	118.1	1.31	1.30	1.30
Na₃Ca	118.4	120.2	121.4	1.28	1.33	1.30
Na₂Ca₂	127.2	117.5	115.2	1.33	1.29	1.28
NaCa₃	126.2	117.0	116.7	1.32	1.28	1.30
Ca₄	124.9	117.7	117.4	1.31	1.30	1.29

Note: Definitions of α , β , and γ angles and l_1 , l_2 , and l_3 are shown in Figure 2.

The calculated vibrational modes of $(CO_3)^{2-}$ are given in Table 3. The most intense bands in the IR absorption related to asymmetric strengthening vibration are shifted to the higher region and located in the range of 1464–1538 cm^{-1} , depending on the cation environments. The lowest wave number of 1464 cm^{-1} is observed for the $(Na_4)^{4+}(CO_3)^{2-}$ cluster. In the case of the Ca cluster $(Ca_4)^{8+}(CO_3)^{2-}$, the asymmetric stretching vibration band is located at 1524 cm^{-1} . The highest wave number of 1538 cm^{-1} is found for the $(Na_2Ca_2)^{6+}(CO_3)^{2-}$ environments. The asymmetric stretching mode of the non-distorted $(CO_3)^{2-}$ group is the degenerate mode. The splitting of this band into a doublet in the range of 1370–1540 cm^{-1} is attributable to the significant distortion of this group in the scapolite structure. The degenerate bending mode in the region of 660–780 cm^{-1} also has high splitting due to the significant distortion.

The absorption spectra of $(CO_3)^{2-}$ anions were calculated for different Na/Ca ratios (Figure 3a). The main electronic transitions are in the region of 5.4–8.5 eV. As the proportion of sodium increases, the energy corresponding to transitions from the ground b2 to the excited b1 state decreases. Thus, if $(CO_3)^{2-}$ is coordinated by four Ca, the energy of the b2→b1 transition is about 7.0 eV, whereas in the case of coordination by four Na, it decreases to 5.4 eV.

Under excitation of these bands at temperatures below 120 K, luminescence in the region of around 3.1 eV is observed, and it is associated with the radiative decay of exciton-like excitations near the carbonate anions (CO_3^{2-}). At temperatures above 120 K, the luminescence intensity in the region of around 3.1 eV decreases. Concurrently, an absorption band appears in the interval 1.7–2.5 eV, which is associated with the carbonate radical anion ($\text{CO}_3^{\cdot-}$) [18].

The electronic and vibration transition energies of the carbonate radical anion ($\text{CO}_3^{\cdot-}$) are calculated. The geometry of the carbonate radical anions in different cation environments is given in Table 4.

Table 3. The calculated vibrational modes of the carbonate anion (CO_3^{2-}) in various cation environments.

Na			Na_3Ca			Na_2Ca_2		
ν (cm^{-1})	σ	I (a.u.)	ν (cm^{-1})	σ	I (a.u.)	ν (cm^{-1})	σ	I (a.u.)
671	0.000	0.3	664	0.000	0.5	676	0.000	0.4
736	0.000	0.3	753	0.001	0.5	769	0.004	1.4
874	0.004	0.0	870	0.004	0.1	868	0.004	0.1
1064	0.001	12.8	1081	0.006	12.5	1055	0.004	9.7
1402	0.140	4.0	1402	0.171	3.5	1371	0.113	1.9
1464	0.149	2.7	1496	0.140	3.1	1538	0.148	1.0
NaCa_3			Ca_4					
ν (cm^{-1})	σ	I (a.u.)	ν (cm^{-1})	σ	I (a.u.)			
671	0.001	0.3	669	0.001	0.4			
779	0.002	1.9	782	0.002	2.3			
867	0.005	0.0	866	0.005	0.0			
1086	0.002	11.7	1098	0.000	12.8			
1409	0.137	2.1	1436	0.147	0.6			
1526	0.172	1.9	1524	0.172	3.6			

Note: σ is oscillator strength, I is a Raman intensity, a.u. means arbitrary units.

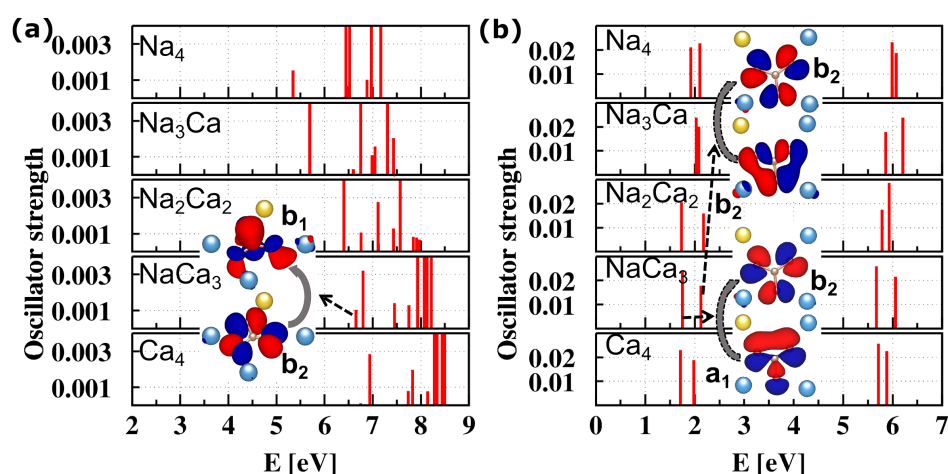


Figure 3. Calculated oscillator strengths for (CO_3^{2-}) (a) and ($\text{CO}_3^{\cdot-}$) (b) in scapolite. Irreducible representations of molecular orbitals are given with respect to C_{2v} point group.

Table 5 shows the energies of electronic transitions in the ($\text{CO}_3^{\cdot-}$) radical anion, which lie in the range from 1.7 to 2.2 eV. The calculated absorption spectra are given in Figure 3b. Additionally, the presence of an unpaired electron leads to the appearance of an ESR signal. The components of the g-factor tensor are also provided in the table. The components of g-tensor are $g_{zz} = 2.016$ – 2.023 , $g_{yy} = 2.012$ – 2.016 , and $g_{xx} = 2.007$.

Table 4. The geometry of the $(\text{CO}_3)^{-}$ radical anion in various cation environments.

	α	β	γ	$l1$	$l2$	$l3$
Na₄	117.9	120.6	121.5	1.27	1.27	1.28
Na₃Ca	117.0	120.3	122.6	1.29	1.28	1.28
Na₂Ca₂	122.1	119.3	118.6	1.30	1.29	1.28
NaCa₃	121.1	119.7	119.3	1.29	1.28	1.28
Ca₄	123.2	118.6	118.2	1.30	1.29	1.29

Note: The definitions of α , β , and γ angles and $l1$, $l2$, and $l3$ are in Figure 2.

Table 5. Energies of electronic transitions, oscillator strength, and g-factor values for the $(\text{CO}_3)^{-}$ radical anions in various environments of Na and Ca.

	E (eV)	σ	g_{xx}	g_{yy}	g_{zz}
Na₄	1.92; 2.01	0.02	2.0057	2.0149	2.0159
Na₃Ca	2.03; 2.08	0.02	2.0056	2.0120	2.0185
Na₂Ca₂	1.73; 2.18	0.02	2.0069	2.0122	2.0218
NaCa₃	1.75; 2.12	0.02	2.0070	2.0136	2.0227
Ca₄	1.71; 1.97	0.02	2.0072	2.0161	2.0213

Note: σ is oscillator strength of the electronic transitions in the $(\text{CO}_3)^{-}$ radical anion.

The calculated parameters of Raman bands are given in Table 6. $(\text{CO}_3)^{-}$ radical anions have a low oscillator strength in the IR absorption spectra. However, in the Raman spectra, active symmetric modes are observed in the region of $1063\text{--}1190\text{ cm}^{-1}$. The first component of asymmetric doublet is in the range of $1121\text{--}1216\text{ cm}^{-1}$. The second component of the doublet is located in the range of $1168\text{--}1242\text{ cm}^{-1}$.

Table 6. Raman shifts and intensities of Raman bands for the $(\text{CO}_3)^{-}$ radical anions in various environments of Na and Ca.

Na₄		Na₃Ca		Na₂Ca₂		NaCa₃		Ca₄	
ν (cm^{-1})	I (a.u.)	ν (cm^{-1})	I (a.u.)	ν (cm^{-1})	I (a.u.)	ν (cm^{-1})	I (a.u.)	ν (cm^{-1})	I (a.u.)
331	27	381	43	342	36	380	32	365	28
461	8	495	15	534	54	456	10	482	29
1083	71	1079	69	1043	46	1062	81	1047	96
1216	246	1163	166	1152	230	1135	235	1121	271
1242	277	1288	356	1247	292	1256	313	1168	408

Note: I is intensity of Raman bands, a.u. means arbitrary units.

3.1.2. F-Centers

As noted above, the non-radiative decay of exciton-like excitations occurs with the formation of a pair of defects—a hole $(\text{CO}_3)^{-}$ radical anion and an electronic defect, which is most often an F-center. An F-center refers to a vacancy of a halogen anion (chlorine or fluorine) that has captured an electron. In this case, metal clusters of the form of $(\text{Na}_x\text{Ca}_{4-x})^{(7-N)+}$ are formed.

F-centers have absorption bands in the visible region at the spectrum, ranging from 2.47 to 2.85 eV. The position of the bands varies slightly depending on the ratio of sodium to calcium in the cluster. The excited state of the F-center is triply degenerate; therefore, one–three absorption bands can be observed in the absorption spectrum. The presence of an unpaired electron localized on an anion vacancy also leads to the appearance of an ESR signal. Its isotropic g-factor is given in Table 7 along with the position of the lowest energy absorption band, which lies in the region of 2.0005–2.0001. The excited state of F-center has p-like nature and it is triply degenerate. Therefore, two or three bands could be observed in the absorption spectra of the F-center when its environment has low symmetry.

Table 7. Energies of electronic transitions, oscillator strength, and g-factor values for the F-centers in various environments of Na and Ca.

	<i>E</i> (eV)	σ	g-Factor
Na₄	2.28; 2.57; 2.70	0.29	2.0021
Na₃Ca	2.54; 2.77	0.34	2.0013
Na₂Ca₂	2.64; 2.85	0.29	2.0006
NaCa₃	2.52; 2.86	0.30	2.0005
Ca₄	2.68; 2.76	0.35	2.0002

Note: σ is oscillator strength of the electronic transitions in the F-centers.

3.1.3. Polysulfide Radical Anions

The S_3^- radical anion is another well-known blue chromophore in microporous compounds [38]. It causes blue coloration in afghanite, kyanoxalite, marinellite, lazurite, and haüyne [39]. The presence of such radical anions has not yet been reliably detected in scapolites, but their presence is possible in high-temperature sulfur-containing scapolites [40]. The calculated geometrical parameters of the S_3^- radical anion in different cation environments are given in Table 8.

Table 8. The geometry of the S_3^- radical anion in various cation environments.

	α	β	γ	<i>l1</i>	<i>l2</i>	<i>l3</i>
Na₄	110.2	34.9	34.9	3.22	1.96	1.96
Na₃Ca	109.2	35.4	35.4	3.20	1.96	1.96
Na₂Ca₂	106.7	36.7	36.5	3.16	1.97	1.96
NaCa₃	108.4	35.9	35.7	3.18	1.97	1.96
Ca₄	109.0	35.6	35.3	3.19	1.97	1.95

Note: Definitions of α , β , and γ angles and *l1*, *l2*, and *l3* are in Figure 2.

In this work, the energies of vibrational and electronic transitions were calculated from first principles. The results of the calculations of the electronic transitions are given in Table 9. The absorption band responsible for the blue color has a maximum in the region of 2.34 to 2.45 eV. Its position changes slightly depending on the ratio of sodium and calcium in the environment of the S_3^- radical anion. The calculated g-factor values are also shown in the table. The values of the g_{xx} component lie in the region of 2.0015–2.0020, g_{yy} in the region of 2.0359–2.0408, and g_{zz} in the region 2.0497–2.0600.

Table 9. Calculated energies of the lowest energy electronic transitions and g-factor of S_3^- radical anions in various environments of Na and Ca.

	<i>E</i> (eV)	σ	g_{xx}	g_{yy}	g_{zz}
Na₄	2.34	0.05	2.0020	2.0378	2.0590
Na₃Ca	2.41	0.05	2.0017	2.0359	2.0550
Na₂Ca₂	2.42	0.05	2.0013	2.0398	2.0507
NaCa₃	2.37	0.05	2.0015	2.0408	2.0497
Ca₄	2.45	0.05	2.0015	2.0389	2.0531

Note: σ is oscillator strength of the electronic transitions in the S_3^- .

Table 10 shows the calculated positions of the bands in the Raman spectrum associated with S_3^- . The most intense band in the Raman spectra is observed in the region of 593–597 cm^{-1} , depending on the S_3^- environment.

Table 10. Raman shifts and intensities of Raman bands for the S_3^- radical anions in various environments of Na and Ca.

Na ₄		Na ₃ Ca		Na ₂ Ca ₂		NaCa ₃		Ca ₄	
ν (cm ⁻¹)	<i>I</i> (a.u.)	ν (cm ⁻¹)	<i>I</i> (a.u.)	ν (cm ⁻¹)	<i>I</i> (a.u.)	ν (cm ⁻¹)	<i>I</i> (a.u.)	ν (cm ⁻¹)	<i>I</i> (a.u.)
261	5.7	270	6.5	269	6.6	270	7.9	267	8.8
585	67.3	594	55.9	593	47.9	597	53.9	595	38.6
634	6.6	632	6.7	622	8.1	632	5.9	639	18.2

Note: *I* is intensity of Raman bands, a.u. means arbitrary units.

Another sulfide radical anion found in scapolites is S_2^- . Table 11 shows the calculations of the positions of the absorption band and the *g*-factor for S_2^- in different environments of Na and Ca. Depending on the environment, the maximum of the absorption band associated with transitions from the ground state b_{2u} to the excited state b_{2g} changes in the region from 3.25 to 3.45 eV. The table also shows the *g*-factor values for S_2^- . The *g*-factor values lie in the interval 2.20–2.08.

Table 11. Calculated energies of the lowest energy electronic transitions and *g*-factor of S_2^- radical anions in various environments of Na and Ca.

	<i>E</i> (eV)	σ	<i>g</i> _{iso}
Na ₄	3.24	0.05	2.205
Na ₃ Ca	3.37	0.06	2.190
Na ₂ Ca ₂	3.43	0.05	2.130
NaCa ₃	3.42	0.05	2.095
Ca ₄	3.45	0.05	2.086

Note: σ is oscillator strength of the electronic transitions in the S_2^- .

The calculated vibrational modes active in the Raman spectra are given in Table 12. According to calculations, the position of the most intense band in the Raman spectra is in the region of 619–630 cm⁻¹, depending on the cation environment of the S_2^- radical anion.

Table 12. Raman shifts and intensities of Raman bands for the S_2^- radical anion in various environments of Na and Ca.

Na ₄		Na ₃ Ca		Na ₂ Ca ₂		NaCa ₃		Ca ₄	
ν (cm ⁻¹)	<i>I</i> (a.u.)	ν (cm ⁻¹)	<i>I</i> (a.u.)	ν (cm ⁻¹)	<i>I</i> (a.u.)	ν (cm ⁻¹)	<i>I</i> (a.u.)	ν (cm ⁻¹)	<i>I</i> (a.u.)
117	2.3	145	2.9	154	4.1	168	5.3	192	5.3
623	33.1	619	35.8	622	35.2	618	34.0	630	33.7

Note: *I* is intensity of Raman bands, a.u. means arbitrary units.

3.2. Experimental Results

3.2.1. Crystal Structure

The low-symmetrical (space group $P4_2/n$) crystal structure of Sample Sh-1 contains three non-equivalent tetrahedral sites forming an aluminosilicate framework (Figure 4). According to the well-known empirical correlation for the aluminosilicates framework [41], the occupancy of the tetrahedral sites is estimated based on the $\langle T-O \rangle$ distances. The *T1* site, which is characterized by the shortest mean *T1*–O distance of 1.608 Å (Table S3), is completely occupied by Si atoms. The *T2* site is characterized by a $\langle T2-O \rangle$ distance of 1.635 Å and is occupied predominantly by Si with an admixture of Al with a Si:Al ratio of 3:1. The *T3* site with the largest $\langle T3-O \rangle$ distance of 1.695 Å is occupied predominantly by Al atoms (Al:Si = 13:7).

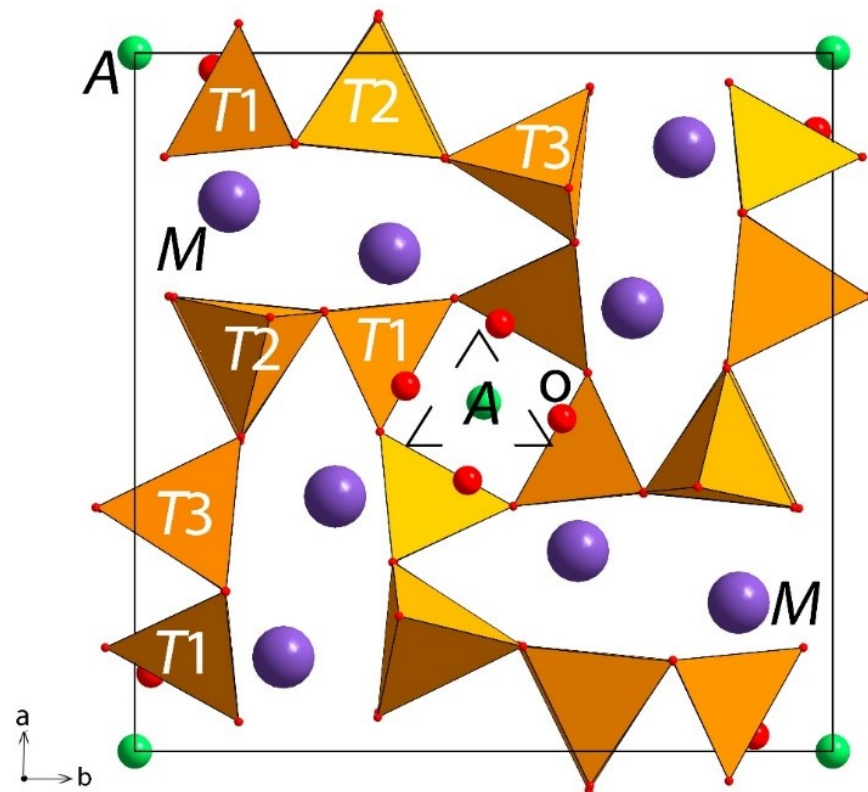


Figure 4. Crystal structure of Sample Sh-1. Positions of atoms belonging to the disordered $(\text{CO}_3)^{2-}$ group around the A site are shown.

The extra-framework cationic M site is occupied by Na (2.8 apfu), Ca (1.0 apfu), and K (0.2 apfu) atoms. The extra-framework anionic A site is predominantly occupied by Cl. However, based on the Fourier residual electron density map (Figure 5), it is possible to localize the oxygen atoms of the $(\text{CO}_3)^{2-}$ group, the presence of which is also in good agreement with the chemical composition, taking into account the well-known correlation for scapolites, $\text{Na}_3 + \text{Si}_2 + \text{Cl} \rightleftharpoons \text{Ca}_3 + \text{Al}_2 + \text{CO}_3$ [3,42]. Due to the presence of Ca^{2+} , which occupies 1/4 of the in the M site, the A site is also 1/4 occupied by the carbon atom of the $(\text{CO}_3)^{2-}$ group, which is disordered due to the action of the four-fold axis (Figure 5). Thus, the refined occupancy of the A site is $\text{Cl}_{0.75}(\text{CO}_3)_{0.25}$. The oxygen atoms belonging to the carbonate anion are characterized by the $\langle \text{C}-\text{O} \rangle$ distance of 1.312 Å and in accordance with the site multiplicities have an occupancy of 0.1875 (Table S2).

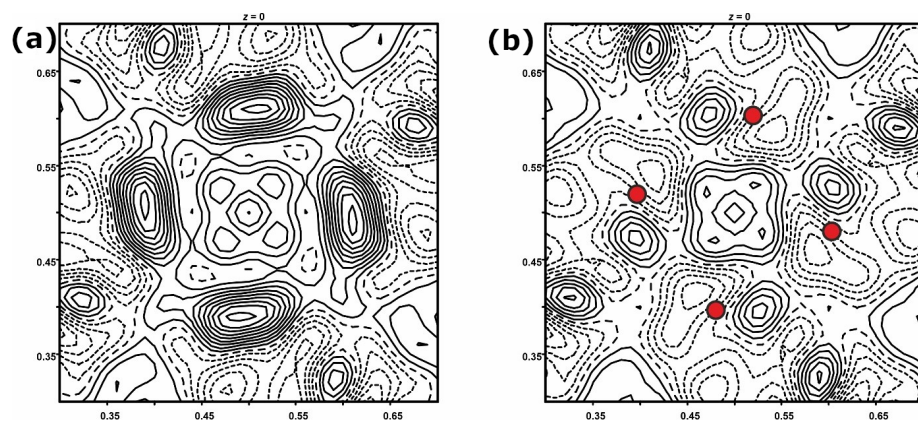


Figure 5. Difference electron density map before (a) and after (b) the refinement of oxygen (red dots). The $(\text{CO}_3)^{2-}$ group is disordered due to the action of the four-fold axis. Intervals between isolines are $0.05 \text{ e} \cdot \text{Å}^{-3}$.

3.2.2. Infrared Spectroscopy

IR spectra of the studied samples are given in Figure 6. The assignment of the IR absorption bands has been made based on our previous data [27] and the results of the ab initio calculations Table 3.

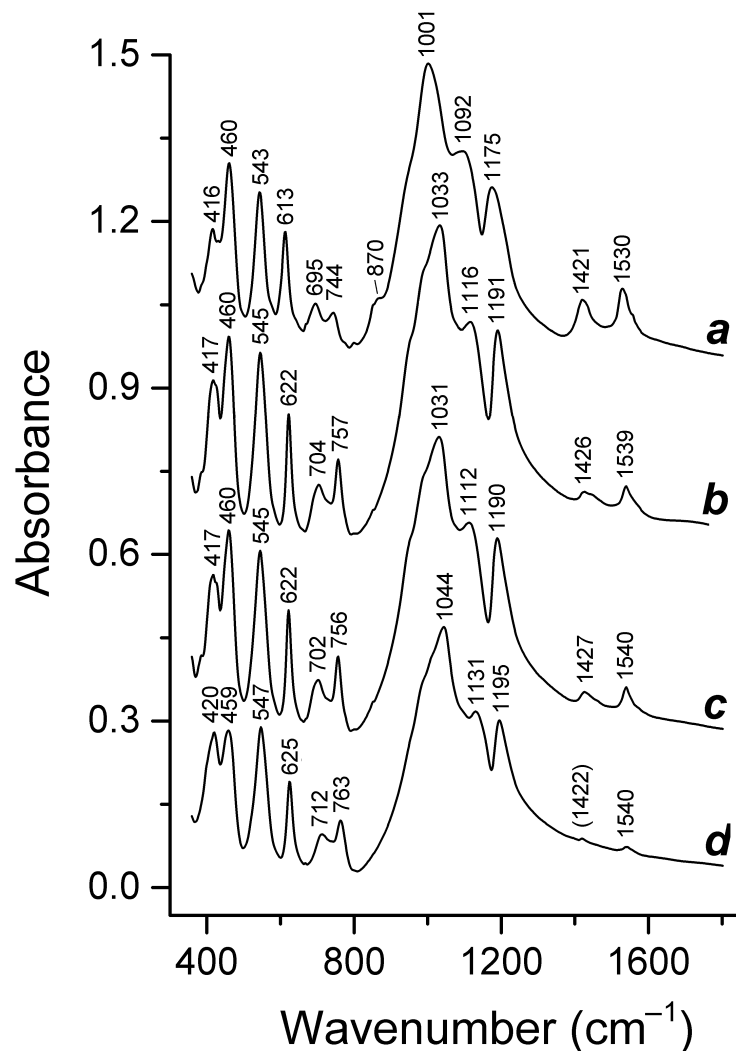


Figure 6. IR spectra of Samples 1366 (a), 2386 (b), 250 (c), and 3614 (d).

No detectable bands are observed in the IR spectra above 1600 cm^{-1} . The doublet in the range of $1420\text{--}1540\text{ cm}^{-1}$ corresponds to the asymmetric stretching vibrations of the $(\text{CO}_3)^{2-}$ anion (degenerate mode). A large splitting of this band indicates a strong distortion of the CO_3 triangle. The shoulder at 870 cm^{-1} in the IR spectrum of Sample 1366 with the highest content of carbonate groups is related to the non-degenerate out-of-plane bending mode of $(\text{CO}_3)^{2-}$.

Bands in the ranges of $1000\text{--}1200$, $540\text{--}760$, and $410\text{--}460\text{ cm}^{-1}$ correspond to $T\text{--O}$ stretching, O--T--O bending, and $T\text{--O--T}$ bending vibrations of the aluminosilicate framework ($T = \text{Si, Al}$). Bands of admixed $(\text{SO}_4)^{2-}$ groups are not observed in the IR spectra because of their overlapping with strong bands of the framework.

3.2.3. Raman Spectroscopy

Raman spectra of scapolites are more informative than their IR spectra. Raman spectra of the studied marialite and meionite samples are given in Figure 7 and Figure 8, respectively. The assignment of the Raman bands has been made based on our previous data [27,43] and results of the ab initio calculations.

All Raman spectra obtained in this work contain series of bands in the range of 1480–3300 cm^{-1} which are typical for hydrated proton complexes, including hydronium cation H_3O^+ or the complex $\text{H}_2\text{O}\cdots\text{H}^+$, involved in extremely strong hydrogen bonds [43]. The strongest bands in this region are observed in the Raman spectrum of Sample 2386, which has a hydrothermal origin and is characterized by a significant deficiency of extra-framework metal cations.

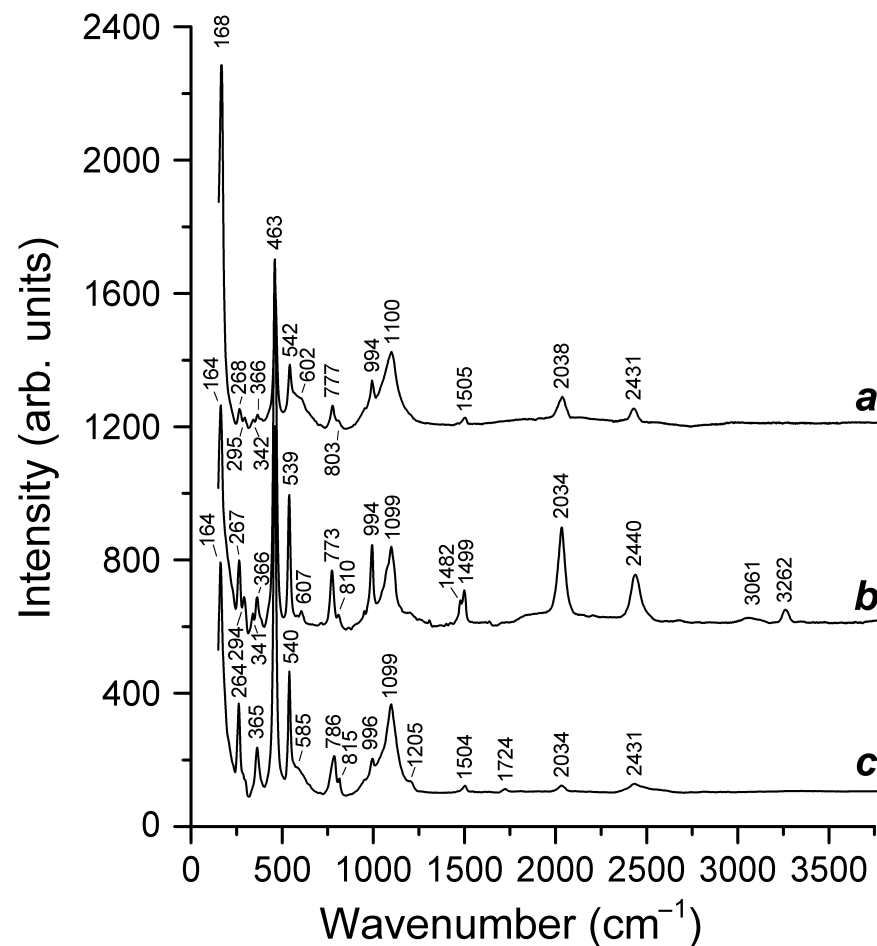


Figure 7. Raman spectra of marialite Samples 250 (a), 2386 (b), and 3614 (c).

Raman spectra of Sample S-22 are given in Figure 9. The weak bands at 591 and 625 cm^{-1} are found in the initial sample. After annealing at 950 $^{\circ}\text{C}$, the intensity of these bands is increased.

Bands in the ranges of 1094–1100 and 985–996 cm^{-1} are due to symmetric stretching vibrations (non-degenerate modes) of $(\text{CO}_3)^{2-}$ and $(\text{SO}_4)^{2-}$, respectively. As noted earlier [27], the high frequencies of the bands of symmetric stretching vibrations of $(\text{CO}_3)^{2-}$ anions may be caused by steric hindrances. In the Raman spectra of marialites, this band is broadened which could be a result of unresolved splitting due to a diversity of the local environment of the $(\text{CO}_3)^{2-}$ anion (different combinations of the Ca^{2+} and Na^+ cations: see Table 3). The band at 1098 cm^{-1} in the Raman spectrum of Sample 1366 corresponds to the local situation $[\text{Ca}_4(\text{CO}_3)]^{6+}$ whereas the lowered wave number of 1094 cm^{-1} for Sample 54413 may be due to a minor admixture of the $[\text{NaCa}_3(\text{CO}_3)]^{5+}$ clusters.

The band of $T-O-T$ bending vibrations at 456 cm^{-1} is overlapping with the strong band of stretching vibrations of the $[\text{Na}_4\text{Cl}]^{3+}$ cluster; the band in the range of 259–268 cm^{-1} corresponds to the bending mode of this cluster.

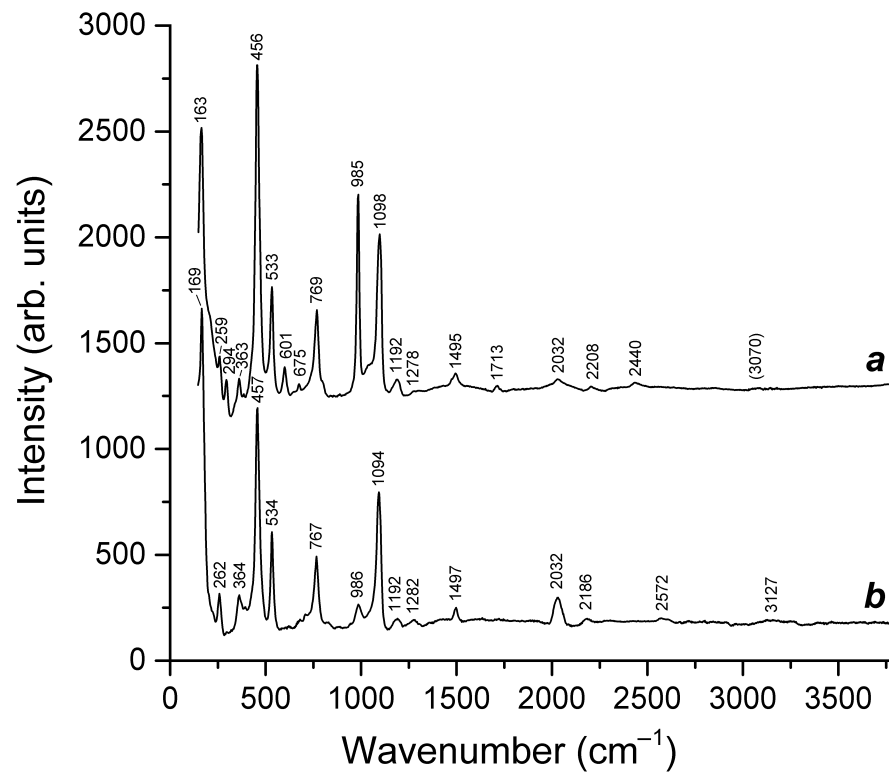


Figure 8. Raman spectra of meionite Samples 1366 (a) and 54413 (b).

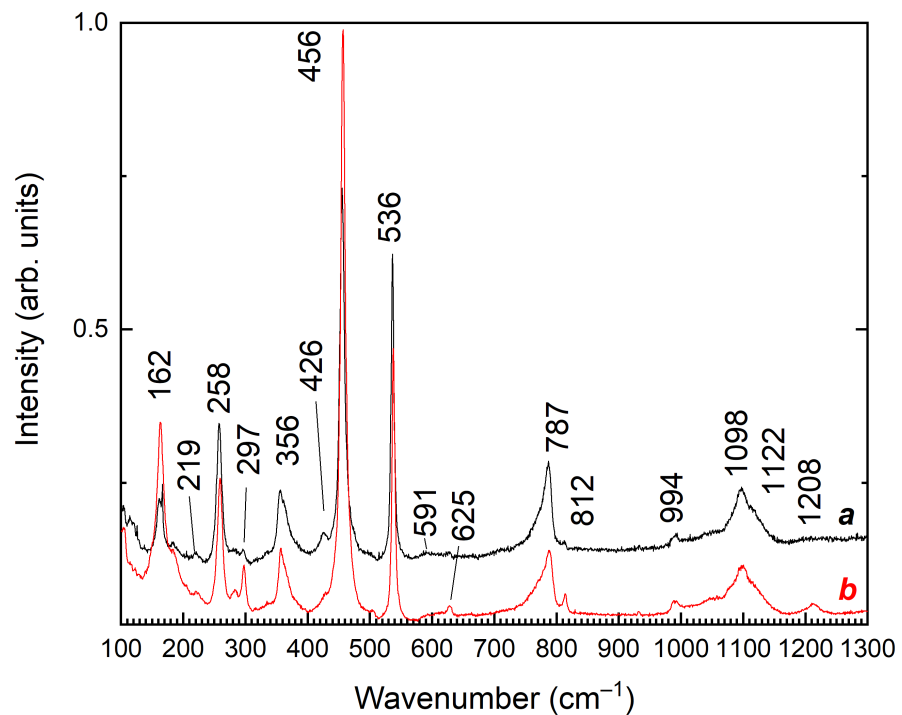


Figure 9. Raman spectra of Sample S-22 measured at $-190\text{ }^{\circ}\text{C}$: initial (a) and annealed during 3 h at $950\text{ }^{\circ}\text{C}$ (b).

In the characteristic wave number range of the $(\text{CO}_3)^{\cdot-}$ radical anion ($1110\text{--}1290\text{ cm}^{-1}$), the bands at 1192 and 1280 cm^{-1} are observed in the Raman spectra of the studied meionites. The former value is close to the calculated wave number for the local situation $[\text{Ca}_4(\text{CO}_3^{\cdot-})]^{7+}$ Table 6.

The band at 294–295 cm^{-1} is observed in the Raman spectra of samples with detectable contents of F and is absent in the other spectra. Thus, this band is to be assigned to the F^- translational mode. Bands in the range of 600–610 cm^{-1} may be due to stretching vibrations of the S_2^- radical anion [27] (see Table 12). The shoulder at 585 cm^{-1} in the Raman spectrum of violet marialite (Sample 3614) can be assigned to the S_3^- radical anion, which is a blue or bluish-violet chromophore [27] (see Table 10). All other bands below 900 cm^{-1} are attributable to the bending vibrations of the framework and the lattice modes, involving the translation and rotation of extra-framework components.

3.2.4. Electronic Spectroscopy of Scapolites

The absorption spectra of various scapolites studied in this work are presented in Figure 10.

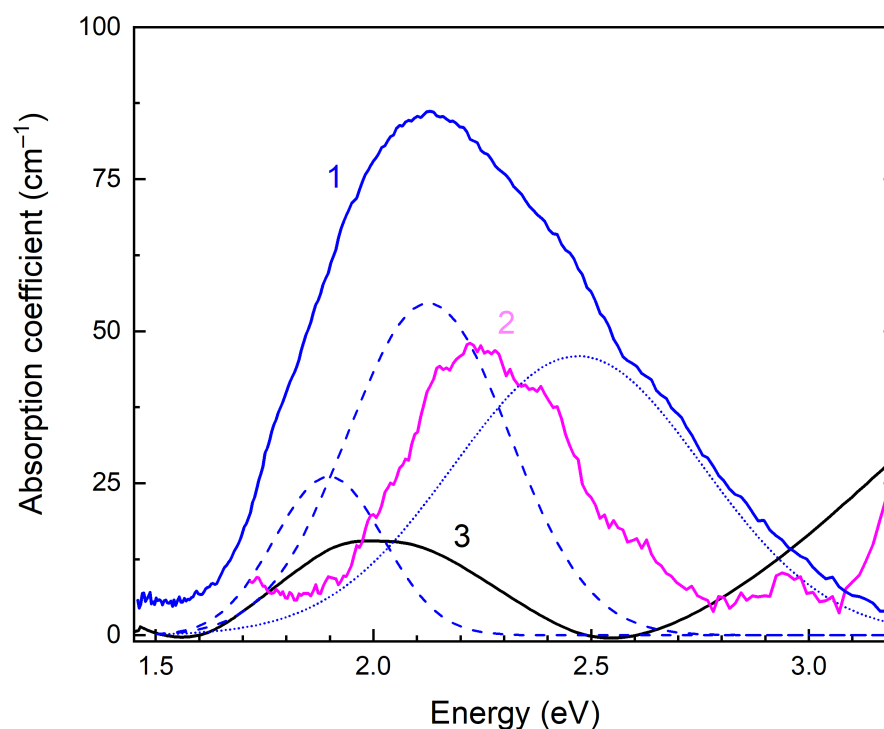


Figure 10. Absorption spectra of scapolites 11/446 (1), 3614 (2), and 1366 (3). The dotted lines show the decomposition of spectrum (1) into components. Dashed lines show bands associated with $(\text{CO}_3)^-$ dotted curve is a band associated with F centers.

The sample of the blue scapolite–glaucolite, Sample 11/446, from Slyudyanka, has a wide asymmetric absorption band in the region of 2.0 eV (Figure 10, curve 1). Three components can be distinguished in the spectrum, with maxima at 1.88, 2.13, and 2.5 eV.

In the absorption spectrum of purple Sample 3614, an absorption band in the region of 2.3 eV is observed (Figure 10, curve 2). It also has a complex structure. In the ESR spectrum of this sample, the highest intensity is a signal consisting of 13 lines located at a distance of about 3.1 mT with a g -factor of approximately 2.002, and a weak band with a g -factor of 2.013 can also be identified (Figure 11a).

Sample 1366 has a bluish color (Figure 10, curve 3). In the absorption spectrum of this sample, a wide asymmetric band in the region of 1.6–2.5 eV can also be distinguished. An ESR signal is observed in the region of 2.015 (Figure 11b) for this sample.

In the absorption spectrum of Sample S-22, a wide band with a maximum in the region of 2.30 eV is observed Figure 12a. When the sample is heated for two hours at a temperature of 950 °C, this band does not completely disappear, unlike other marialites and meionites. The color intensity decreases, and a band with a maximum of 2.40 eV appears in the absorption spectrum. If this heated sample is then subjected to X-ray irradiation, then the

original color is partially restored. However, when irradiated with short-wave ultraviolet light from a low-pressure mercury lamp with a wavelength of 254 nm, the sample turns yellow. The intensity of the band in the region of 2.40 eV decreases, and the high-energy edge in the spectrum increases significantly.

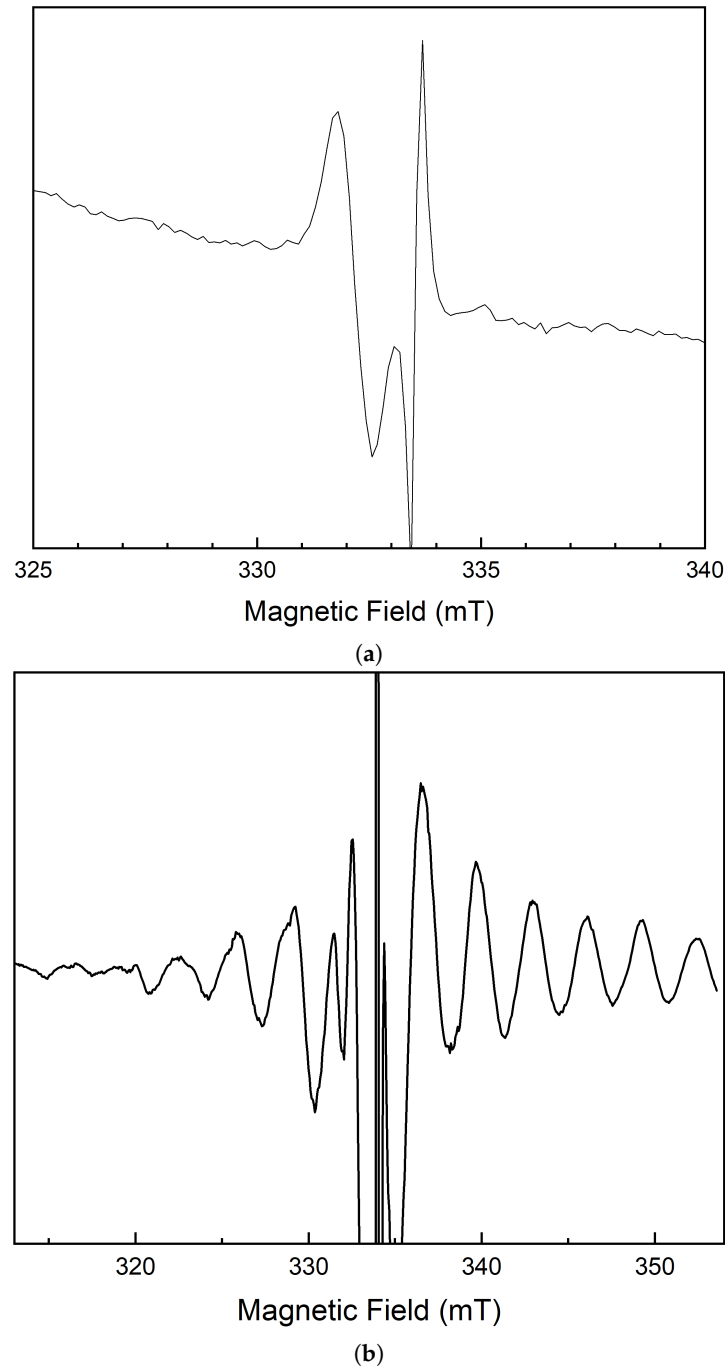


Figure 11. ESR spectra of the 1366 (a) and 3614 (b) samples.

In the ESR spectrum of the initial Sample S-22, an intense ESR signal with a g -factor of 2.002, as well as one with 2.018, and a weak signal with a g -factor in the region of 2.051 are observed (Figure 12b, curve 1). In the heated sample, the intensity of the ESR signal with a g -factor of 2.051 increases, and in the sample irradiated with short-wave ultraviolet light from a low-pressure mercury lamp, the intensity of the signal with a g -factor of 2.051 decreases, but an ESR signal with g -factor of 2.017 appears (Figure 12b, curve 2).

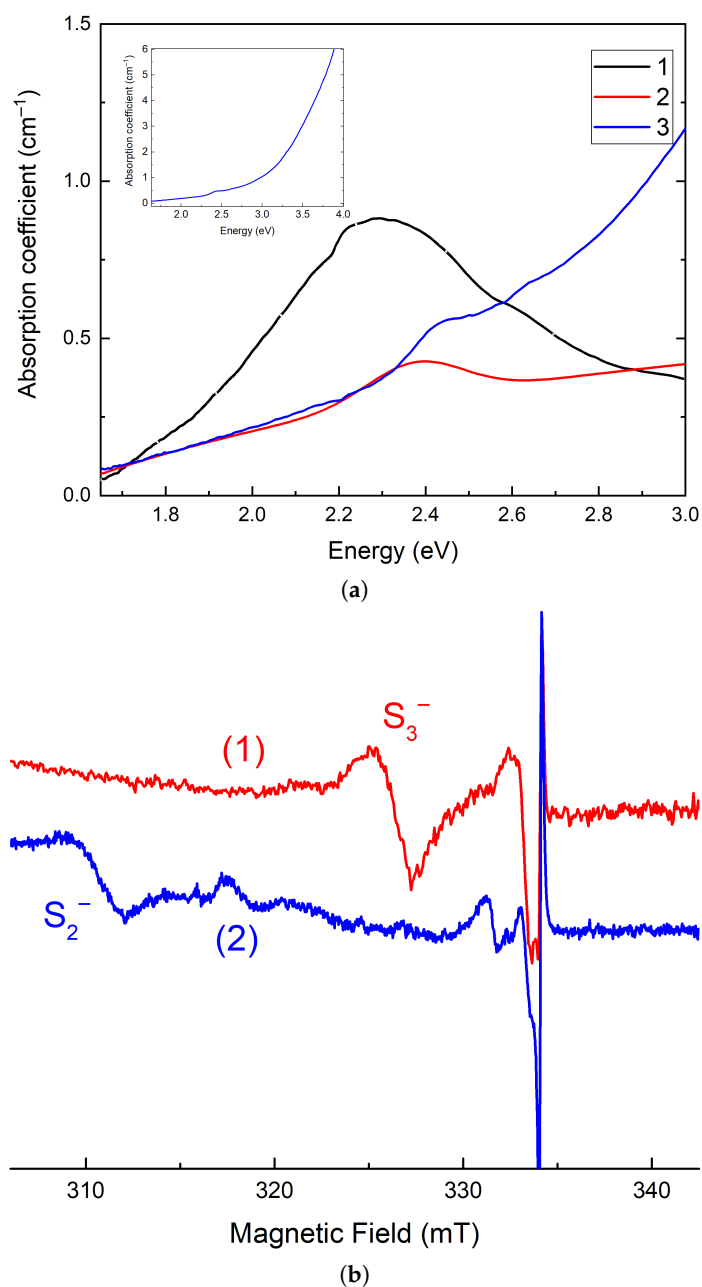


Figure 12. Absorption spectra of Sample S-22 (a): curve 1 is the initial sample, curve 2 is the absorption of the heated at 950 °C Sample S-22, and curve 3 is the heated Sample S-22 after irradiation of 256 nm UV lamp. In sub-figure (b), the ESR spectra of the heated (curve 1) and then irradiated (curve 2) for Sample S-22 are given.

In Samples 250, 1366, 418, and S-22, luminescence with a maximum in the region of 580 nm was observed (Figure 13a). The observed luminescence has a vibrational structure characteristic of S_2^- radical anions. The position of the luminescence band weakly depends on the sample. The Figure 13 shows the luminescence spectra for samples of the meionite (Figure 13a, curve 1) and marialite types (Figure 13a, curve 2). Heating at a temperature of 950 °C leads to an increase in the intensity of this luminescence.

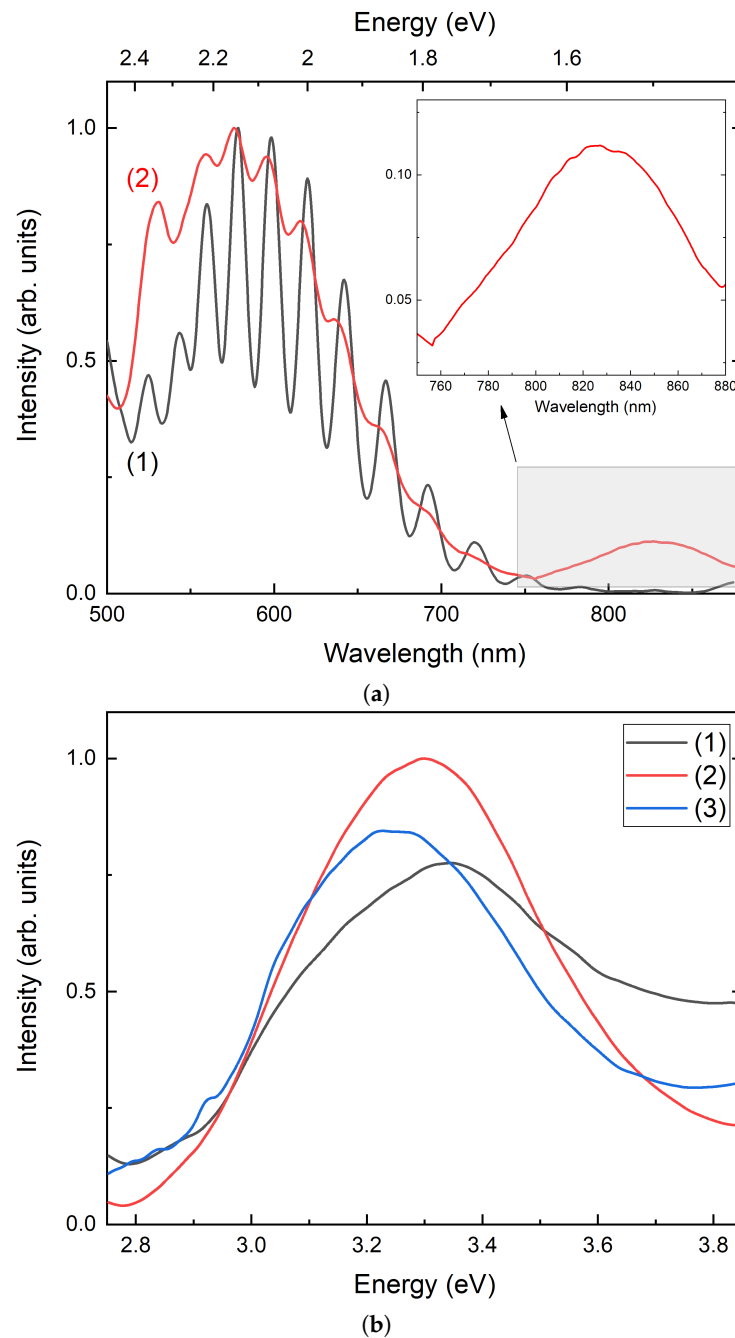


Figure 13. Luminescence (a) and excitation (b) spectra. Curves 1 and 2 in Figure 13a correspond, respectively, to initial Sample 418 and Sample 2 heated at 950 °C and then irradiated with 256 nm UV lamp Sample S-22 under 3.3 eV excitation. The inset shows luminescence spectrum of Sample S-22 heated and then irradiated with 4.3 eV radiation. Curves 1, 2, and 3 in Figure 13b correspond to initial Sample 412, Sample 1366 heated at 950 °C, and heated Sample S-22.

The excitation spectrum exhibits an intense band in the region of 3.20–3.40 eV, as well as higher energy bands in the region of 4.30 and 5.15 eV Figure 13b. The position of the maximum of the low-energy band depends on the relation between Cl/CO₃. In meionites end-members—for example in Sample 418—this occurs in the highest energy region, at about 3.35 eV. In heated Samples 1366 and 250, the band maximum is in the region of about 3.30 eV. In Sample S-22, the band maximum is located in the region of about 3.25 eV.

In Sample S-22, that was heated and then irradiated with short-wave ultraviolet light, upon excitation in the region of 4.30 eV, a luminescence band with a maximum of 830 nm appears in the near-infrared region (in the inset of Figure 13).

4. Discussion

There is a good agreement between the results of the theoretical calculations and the experimental spectroscopic data obtained in this work. In particular, the carbonate anion tends to be coordinated by calcium ions and chlorine by sodium ions, but the IR absorption spectra show that intermediate local situations also occur in nature.

The tetrahedral frameworks in the crystal structures of scapolite-group minerals is related to the large family of compounds formed by the condensation of the tetrahedral layers with the apophyllite-type (4^18^1) topology [44,45], but this is characterized by the unique sheet of stereoisomerism [46]. A topological analysis of the tetrahedral framework was performed based on a natural tiling [47] (partition of the crystal space by the smallest cage-like units) analysis of the 3D cation nets using the ToposPro software [48]. The natural tiling consists of three natural tiles $[5^2.8^3]_4[4^2.5^4]_2[4^2.8^4]$ (Figure 14). It should be noted that the tile $[4^2.8^4]$ has been found in the framework of DFT type (the type of material is DAF-2, $(C_2H_8N_2)_2[Co_4P_4O_{16}]$ [49]); meanwhile, tile $[5^2.8^3]$ is present in the heteropolyhedral MT-framework in the crystal structure of seidite-(Ce) [50]. DAF-2 and seidite-(Ce) both belong to 2D and 3D zeolites, with a modulus based on tetrahedral nets with the apophyllite-type topology [45]. This indicates the presence of a topological relation with the scapolite-group minerals.

As noted above, for minerals of the scapolite group belonging to the marialite–meionite series, a direct correlation has been established between the valence of cations at the *M* site and anions at the *A* site as well as in the Si/Al ratio [3,42,51]. Thus, from the data of the chemical analyses of the studied samples, it is clear that, with a decrease in the total amount of monovalent cations (Na and K), the content of Cl also decreases proportionally—whereas the amount of $(CO_3)^{2-}$ increases.

We observed a decrease in symmetry (to space group $P4_2/n$) for all studied samples where the amount of monovalent extra-framework cations (the sum of Na + K) was 3.1 apfu or less (the minimum value in the studied samples was about 2.7 apfu, and the amount of Ca^{2+} was 0.9–1.3 apfu); meanwhile, at a sum of Na + K above 3.1 apfu, a high-symmetry space group $I4/m$ is realized. Thus, we can conclude that the decrease in marialite symmetry to the space group $P4_2/n$ occurs at relatively high (≥ 0.25) occupancies of the *M* site with calcium and, accordingly, high $(CO_3)^{2-}$ contents.

The decrease in symmetry can be explained by the partial occupation of the *A* site by a disordered carbonate group, as well as by an uneven change in the size of the tetrahedra of the aluminosilicate framework due to the changing Si/Al ratio. This assumption is in good agreement with previously established correlations between the chemical compositions and structures of scapolites from other deposits [4].

The assumption that the carbonate radical anion $(CO_3)^{\cdot-}$ is responsible for the purple and blue colors of scapolites was made in [16]. However, later, this was questioned in several works [12,19], which suggested that the purple and blue color of scapolites is caused by the presence of $O^{\cdot-}$ centers in the halogen position or $S^{\cdot-}$ center in the Cl^- position [52]. Thus, the mechanism by which such coloring occurs remains unclear.

In [18], it was shown that the observed absorption in the region of 2.000 eV and the ESR signals at 2.018 and 2.011 are associated with the carbonate radical anions. The excitonic mechanism of their formation described above was also proposed. This coloring mechanism is more probable compared to $O^{\cdot-}$ centers, as the ionization energy of oxygen complexes is significantly higher than that of the halogen ion [53].

Moreover, in [14,22], it was noted that some scapolites acquire a blue color when irradiated with short-wave ultraviolet radiation, which also indicates the exciton mechanism of defect formation and casts doubt on the connection between the blue coloring and $O^{\cdot-}$ anions.

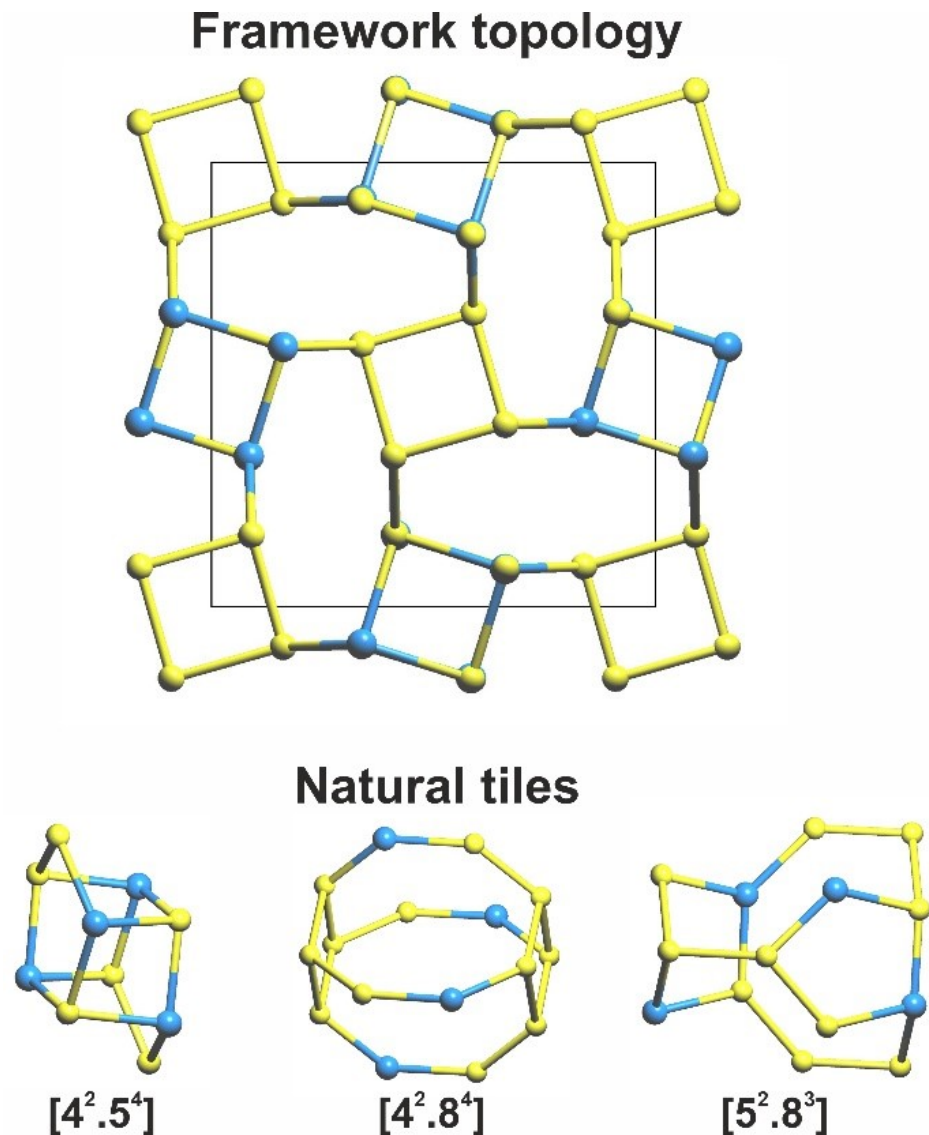


Figure 14. Topological features of the tetrahedral framework in scapolite-group minerals.

The nature of the color of the scapolites studied in this work is considered. In Sample 11/446, the lower energy bands at 1.88 and 2.13 eV are associated with the a1-b2 transitions in the $(\text{CO}_3)^{\cdot-}$ radical anion, and the higher energy band at 2.50 eV is associated with the absorption of F-centers. Comparing the data with the calculations, we can assume that the formation of such radiation defects most likely occurs in the NaCa_3 or Na_2Ca_2 complexes. Sample 418 has a similar absorption spectrum. Furthermore, in Samples 418 and 11/446, an ESR signal with a g-factor of 2.018–2.020 is observed, which is also associated with the presence of $(\text{CO}_3)^{\cdot-}$ centers [18,27].

In purple Sample 3614, the ESR signal with a g-factor of 2.013 is attributed to the $(\text{CO}_3)^{\cdot-}$ radical anions, while the ESR signal with a g-factor of 2.002 is associated with F-centers surrounded by four ^{23}Na ($J = 3/2$). Thus, the absorption band in the region of 2.30 eV is associated mainly with the absorption of F-centers surrounded by four ^{23}Na ions. The experimental results are well correlated with the calculation Table 7. The amount of $(\text{CO}_3)^{\cdot-}$ radical anions in the purple sample is significantly less than that in the F-centers, which determines the purple color of the sample. In this case, molecular complexes with covalent bond $(\text{Cl}_2)^{\cdot-}$ or $(\text{FCl})^{\cdot-}$ can act as hole centers. Their absorption is in the ultraviolet region of the spectrum, so they do not affect the color of scapolites.

In [22], the observed “photochromic” band is also attributed to the combination of $(\text{CO}_3)^{\cdot-}$ and F-centers bands; it cannot be attributed to F-centers absorption only, as

was assumed in this article. The authors' assumption that the wide reflection band is associated precisely with the transition inside the F-center was supported by their ab initio calculations, including the DFT method. In general, our calculation methodology is very similar to that proposed by the authors of [22,54]. This methodology consists of calculating the defect geometry using periodic calculations and the optical spectra using DFT, implemented in the embedded cluster method. Currently, the development of software products has led a situation in which calculation results do not depend on the choice of software package. However, the calculation results very much depend on the choice of a basis for the cluster calculations. In our calculations, the def2 basis was used without any changes; meanwhile, the authors of [22] modified the used basis, apparently in order to bring the calculation results closer to those of the experimental data. This means that their results are more empirical.

Thus, the purple and blue colors of scapolites may be caused by different ratios of carbonate radical anions and F-centers. For example, Cl-rich scapolites (marialites) from Central Pamir have purple colors, but the samples with a sum deficiency that could be compensated for by the carbonate group have a more bluish color [11].

Another strong chromophore in microporous materials is the S_3^- radical anion. According to our calculations, the bands in the region of 580–590 cm^{-1} in the Raman spectra may relate to S_3^- anion radicals. Weak bands in this spectral region were observed in lilac marialites (3614 and S-22), which may indicate the presence of traces of S_3^- in these samples. As noted above, heating most scapolite samples leads to the disappearance of color. However, in Sample S-22, the color is retained. In the Raman spectrum of this sample, weak bands are observed in the region of 580–590 cm^{-1} , which, according to calculations, are associated with S_3^- and/or S_2^- radical anions (Tables 10 and 12). When heated, the intensity of these bands increases. Moreover, in heated Sample S-22, an ESR signal with a g-factor of 2.052 appears, and a weak band remains in the region of 2.40 eV. According to calculations, these bands are associated with S_3^- radical anions Table 9. This sample is from a secondary cavity in pegmatite, which may indicate its relatively high temperature origin. At these temperatures, under certain conditions, the transformation of the sulfate group into sulfide radical anions can occur. This explains the increase in the luminescence intensity of S_2^- radical anions observed in this work, as well as in earlier studies, in heated samples [25,39].

On the other hand, S_3^- centers can also contribute to the observed band in the region of 2.3 eV. According to calculations, absorption of S_3^- radical anions can be observed in this region Table 9. This may also be supported by the fact that, in the Raman spectrum of this sample, there is a weak band in the region of 585–610 cm^{-1} , which, according to calculations, can also be attributed to S_3^- vibrational modes. However, the number of such radical anions is significantly less than F-centers and $(\text{CO}_3)^-$, so they are difficult to detect in ESR spectra.

One of the common reasons for the yellow color of scapolites is the presence of S_2^- radical anions in them. According to calculations, the bands in the region of 615–630 cm^{-1} are associated with these anion radicals. The presence of such bands in the Raman spectrum is usually accompanied by characteristic luminescence. The yellow color appears because the edge of the absorption band is partially in the visible region of the spectrum. When excited in the region of 3.25–3.45 eV, luminescence is recorded, which has long been studied quite widely in scapolites [24].

There is an uncertainty in determining the energy of the transition with the lowest energy. In samples with different ratios of Na and Ca, the position of the maximum of the excitation band changes, as well as the distance between phonon repetitions in the luminescence spectrum [25]. From the calculations carried out in this work, it follows that this may be due to the presence of S_2^- complexes coordinated by different amounts of Na and Ca.

The yellow color of scapolites is thus caused by the presence of S_2^- radical anions. However, irradiation of Sample S-22 with short-wave UV radiation also leads to the

appearance of a yellow color. The ESR signal with g -factor 2.17 in scapolites has been ascribed to $S^{\cdot-}$ centers [55]. However, following the calculations presented in this paper, this signal should instead be attributed to $S_2^{\cdot-}$ radical anions. The increase in the luminescence intensity of $S_2^{\cdot-}$ centers, alongside the appearance of an ESR signal with a g -factor of 2.17—characteristic of $S_2^{\cdot-}$ radical anions—indicates an increase in the concentration of $S_2^{\cdot-}$ centers upon irradiation with UV light. On the other hand, the edge of the absorption band grows in the region of higher energies than the absorption band associated with $S_2^{\cdot-}$ centers, and the luminescence in the IR region also appears upon excitation at 4.30 eV. Previously, similar luminescence was observed in microporous materials and was associated with $(S_3)^{2-}$ centers [56]. Thus, under short-wave UV irradiation, the decomposition of S_3^{2-} complexes to $S_2^{\cdot-}$ may occur on the one hand, and the formation of $(S_3)^{2-}$ anions may occur on the other hand.

Thus, the presence of various colors of scapolites is mainly due to the different ratios of $(CO_3)^{\cdot-}$ radical anions and F-centers. However, $S_3^{\cdot-}$ centers can also produce a purple color. In the color diagram in Figure 15, the color coordinates of scapolites containing various chromophores described above, such as $(CO_3)^{\cdot-}$, F-centers, $S_2^{\cdot-}$, and $S_3^{\cdot-}$ radical anions, are shown. It can be seen from the figure that there are several color trends, corresponding to different ratios between $(CO_3)^{\cdot-}$ and F-centers in scapolites. The trend was drawn based on theoretically calculated absorption bands of $(CO_3)^{\cdot-}$ and F-centers, depending on the relationships between them and taking different oscillator strengths into account.

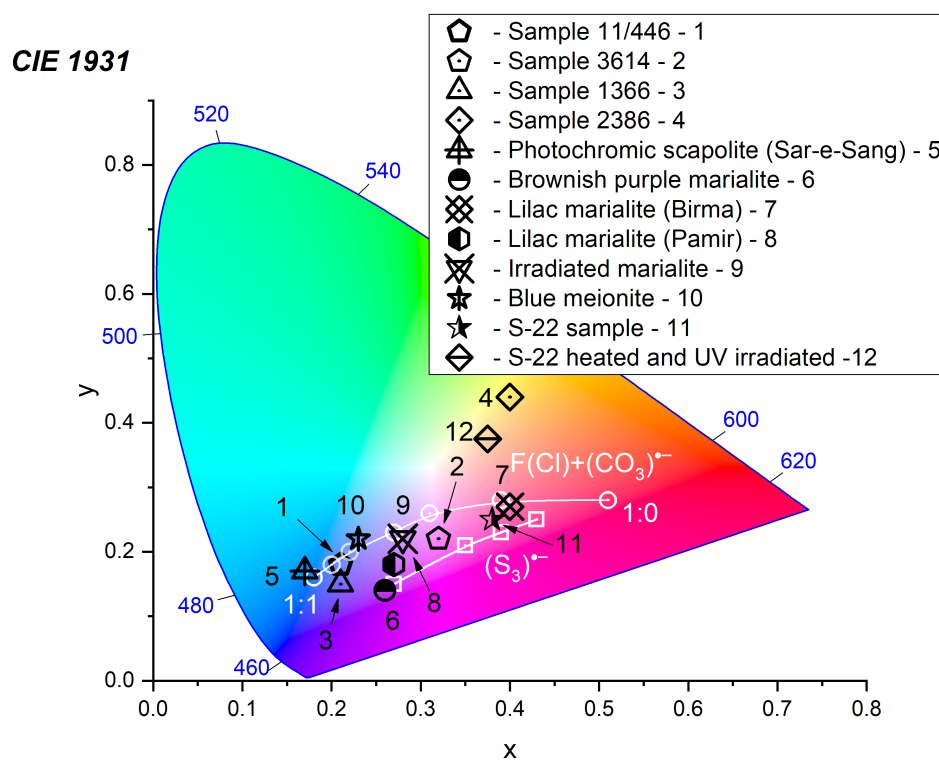


Figure 15. Color space chromaticity diagram for scapolite-group minerals from different sources (black symbols): 1—Sample 11/446; 2—Sample 3614; 3—Sample 1366; 4—Sample 2386; 5—scapolite from [14]; 6—scapolite from [15]; 7, 8, and 9—scapolites from [12]; 10—scapolite from [16]; 11—Sample S-22; 12—Sample S-22 annealed at 950 °C and then irradiated with 256 nm UV lamp. The white lines show the calculated trends for the different relationships between $(CO_3)^{\cdot-}$ and F-centers, where 1:0 shows the color of the scapolite, containing only F-centers, and 1:1 indicates scapolites containing equal concentrations of $(CO_3)^{\cdot-}$ and F-centers. The calculated color trend of the scapolites containing $S_3^{\cdot-}$ radical anions in different Na/Ca coordinations is also shown.

The second trend is based on the results of the calculations of $S_3^{\cdot-}$ radical anions surrounded by Na_4 , Na_3Ca , and Na_2Ca_2 . The extreme point is the average absorption, when

all three possible positions are occupied equally by $S_3^{\cdot-}$ radical anions. The violet–purple Samples 3614 and S-22 lie close to this trend. The Raman spectra of these samples contain the weak band at about $580\text{--}590\text{ cm}^{-1}$, which is related to the $S_3^{\cdot-}$ radical anions—according to the ab initio calculations. The color of these samples is formed $S_3^{\cdot-}$ radical anions together with F-centers and $(CO_3)^{\cdot-}$. The colors of some of the scapolites studied earlier are close to those in the $S_3^{\cdot-}$ trend [12,15]. The presence of $S_3^{\cdot-}$ and $S_2^{\cdot-}$ radical anions in scapolites could be an indicator of high-temperature or high-pressure metamorphic processes. The high-temperature [57] and high-pressure scapolites [58] demonstrate the weak bands in the region of $580\text{--}620\text{ cm}^{-1}$.

The colors of the scapolites studied in this work correspond well to the calculated trends. Sample 3614 lies somewhat below the trend, since it may contain—in addition to $(CO_3)^{\cdot-}$ and F-centers— $S_3^{\cdot-}$ radical anions. The data in the literature are also relatively well distributed between the two trends. It is worth noting that $S_3^{\cdot-}$ radical anions will cause more violet colors to occur in comparison to the pairs of radiation defects $(CO_3)^{\cdot-}$ and F-centers.

5. Conclusions

The variety of colors of scapolites from purple to blue is mainly attributable to pairs of radiation-induced defects. The most widespread pair of defects is the presence of a carbonate radical anion $(CO_3)^{\cdot-}$ combined with the vacancy of an extra-framework anion that has captured an electron (an F-center). F-centers have higher energy absorption bands in the region of 2.3–2.7 eV. ESR signals from F-centers have g-factors of about 2.000. $(CO_3)^{\cdot-}$ carbonate radical anions have wide absorption bands in the region of 1.5–2.5 eV, depending on the cation environment. Furthermore, $(CO_3)^{\cdot-}$ carbonate radical anion demonstrates strong ESR signals with a g-factor of about 2.015. The large amount of $(CO_3)^{\cdot-}$ carbonate radical anions could be also detected in Raman spectra. If the number of such centers is approximately equal, then scapolites will have a blue color. If there are more F-centers than $(CO_3)^{\cdot-}$ carbonate radical anions, the color will shift to purple.

Another less common violet chromophore is the $S_3^{\cdot-}$ radical anion. In some samples, such radical anions were discovered in scapolites for the first time in this work. The $S_3^{\cdot-}$ radical anion demonstrates an absorption band in the region of 2.3–2.4 eV—together with an ESR signal with a g-factor of 2.036–2.041 and a Raman peak in the region of $585\text{--}595\text{ cm}^{-1}$. Scapolites containing an $S_3^{\cdot-}$ -chromophore have a more violet color than scapolites that are colored with $(CO_3)^{\cdot-}$ carbonate radical anions and F-centers.

The presence of $S_2^{\cdot-}$ radical anions in scapolites leads to a yellow color. They have an absorption band at about 3.2–3.5 eV and a Raman peak in the region of $620\text{--}630\text{ cm}^{-1}$. The ESR signal from $S_2^{\cdot-}$ radical anions has g-factor lying in the region of 2.09–2.20. The luminescence band attributed to $S_2^{\cdot-}$ radical anions is found at about 600 nm, with a prominent vibrational structure.

The position of the UV–Vis–NIR and IR absorption bands of extra-framework carbonate anions $(CO_3)^{2-}$, carbonate radical anions $(CO_3)^{\cdot-}$, F-centers, sulfide radical anions $S_3^{\cdot-}$, and $S_2^{\cdot-}$ depends on the cations surrounding them (Na/Ca ratio), which can also lead to variations in the shades of scapolites, as well as to the threshold energy of formation of radiation defects in scapolites.

Supplementary Materials: The following supporting information can be downloaded at: <https://www.mdpi.com/article/10.3390/min14090937/s1>, The Table S1 Crystal parameters, data collection and structure refinement details for Sample Sh-1, Table S2 Fractional site coordinates, equivalent displacement parameters (U_{eq} , Å²) of atoms and site multiplicities (Q) and composition for Sample Sh-1, Table S3 Selected bond lengths (Å) in Sample Sh-1 and.xyz input files for ab initio calculations are provided in the Supplementary Materials.

Author Contributions: Conceptualization, I.V.P., N.V.C. and R.S.; methodology, N.V.C., A.B. (Alexander Bogdanov), R.S. and S.M.A.; software, A.B. (Alexander Bogdanov); validation, A.M., E.P. (Ekaterina Popova) and I.V.P.; formal analysis, N.V.C., R.S., A.B. (Anastasiia Babkina) and S.M.A.; investigation, R.S., A.B. (Alexander Bogdanov), N.V.C., M.F.V., A.B. (Anastasiia Babkina), S.M.A., G.I. and E.P. (Elizaveta Pankrushina); resources, I.V.P., N.V.C. and A.A.Z.; data curation, A.M., R.S. and N.V.C.; writing—original draft preparation, R.S., N.V.C. and G.I.; writing—review and editing, N.V.C., R.S. and I.V.P.; visualization, R.S., N.V.C. and G.I.; supervision, I.V.P. and N.V.C.; project administration, I.V.P. All authors have read and agreed to the published version of the manuscript.

Funding: The UV–Vis–NIR spectroscopy, ESR, Raman spectroscopic studies, and embedded cluster ab initio calculations were supported by the Russian Science Foundation (grant No. 22-17-00006 <https://rscf.ru/project/22-17-00006/> (accessed on 10 September 2024), for R.S., N.V.C., M.F.V., and I.V.P.). The VASP and CP2K ab initio calculations and thermal and radiation conversion were supported by the project 0284-2021-0004 (Materials and Technologies for the Development of Radiation Detectors, Luminophores, and Optical Glasses). Data on infrared spectra and chemical compositions were obtained in accordance with the state task by Russian academy of science (state registration number: AAAA-A19-119092390076-7). X-ray structure analysis was supported by the state task of the Russian Federation, state registration number 122011300125–2 (S.M.A., G.I.). Raman spectra of Sample S-22 were measured with support of the task 123011800012-9 (Elizaveta Pankrushina).

Data Availability Statement: The Raman spectra measured in the article are available in ArDI open access database [59].

Acknowledgments: The authors wish to thank the Isotope-geochemical research center for Collective Use (A. P. Vinogradov Institute of Geochemistry of the Siberian Branch of the Russian Academy of Sciences, the research center for Collective Use “Geoanalitik” shared research facility of the IGG UB RAS, and “Academician V.M. Matrosov” computational cluster for the performing calculations.). The authors also thank to T. A. Radomskaya for the sample 11/446 photo.

Conflicts of Interest: The authors declare no conflicts of interest.

References

1. Hassan, I.; Buseck, P.R. HRTEM characterization of scapolite solid solutions. *Am. Mineral.* **1988**, *73*, 119–134.
2. Teertstra, D.K.; Sherriff, B.L. Scapolite cell-parameter trends along the solid–solution series. *Am. Mineral.* **1996**, *81*, 169–180. [[CrossRef](#)]
3. Seto, Y.; Shimobayashi, N.; Miyake, A.; Kitamura, M. Composition and $I4/m-P4_2/n$ phase transition in scapolite solid solutions. *Am. Mineral.* **2004**, *89*, 257–265. [[CrossRef](#)]
4. Sokolova, E.; Hawthorne, F.C. The crystal chemistry of the scapolite-group minerals. I. Crystal structure and long-range order. *Can. Mineral.* **2008**, *46*, 1527–1554. [[CrossRef](#)]
5. Sokolova, E.; Kabalov, Y.; Urusov, V. The crystal chemistry of the scapolite: Investigation of the marialite–meionite solid solution series by means of the Rietveld method. *Probl. Crystallogr.* **1999**, *5*, 196–227. (In Russian)
6. Sherriff, B.L.; Sokolova, E.V.; Kabalov, Y.K.; Jenkins, D.M.; Kunath-Fandrei, G.; Goetz, S.; Jager, C.; Schneider, J. Meionite: Rietveld Structure-Refinement, ^{29}Si MAS and ^{27}Al Satras Nmr Spectroscopy, and Comments on the Marialite Meionite Series. *Can. Mineral.* **2000**, *38*, 1201–1213. [[CrossRef](#)]
7. Antao, S.M.; Hassan, I.; Wang, J.; Lee, P.L.; Toby, B.H. State-of-the-Art High-Resolution Powder X-ray Diffraction (Hrpxrd) Illustrated with Rietveld Structure Refinement of Quartz, Sodalite, Tremolite, and Meionite. *Can. Mineral.* **2008**, *46*, 1501–1509. [[CrossRef](#)]
8. Yuan, P.; Zhao, Y.; Xu, B.; Shen, J. A Study on the Mineralogy and Volatile Fraction of Scapolite from Mogok, Myanmar. *Crystals* **2022**, *12*, 1779. [[CrossRef](#)]
9. Kostov-Kytin, V.; Kadiyski, M.; Nikolova, R. Further on the Choice of Space Group for Scapolite Group Members and Genetic Considerations about the Si–Al Ordering in Their Framework Construction. *Minerals* **2024**, *14*, 556. [[CrossRef](#)]
10. Bokiy, G.; Borutsky, B.E. *Feldspatoids. Mineraly*; Nauka: Moscow, Russian, 2003; Volume 5, pp. 282–384. (In Russian)
11. Litvinenko, A.; Moiseeva, S.; Odinaev, S.A.; Utenkov, V. Geology of the Chernogorskoe Gem-Quality Scapolite Deposit (Central Pamirs, Tajikistan). *Geol. Ore Depos.* **2019**, *61*, 481–493. [[CrossRef](#)]
12. Zolotarev, A. Gem scapolite from Eastern Pamir and some general features of constitution of scapolites. *Zap. Vsesoyznogo Mineral. Obs. (Proc. Sov. Mineral. Soc.)* **1993**, *122*, 90–102. (In Russian)
13. Balmer, W.A.; Hauzenberger, C.A.; Fritz, H.; Sutthirat, C. Marble-hosted ruby deposits of the Morogoro Region, Tanzania. *J. Afr. Earth Sci.* **2017**, *134*, 626–643. [[CrossRef](#)]
14. Allen, T.; Renfro, N.; Nelson, D. Tenebrescent irradiated scapolite. *Gems Gemol.* **2014**, *50*, 91.
15. Choudhary, G. Purple scapolite. *Gems Gemol.* **2015**, *51*, 203.

16. Taran, M.; Tarashchan, A.; Platonov, A.; Bagmut, N.; Skrigitil, A. Spectroscopic investigation of gem scapolites of Eastern Pamir. *Zap. Vsesoyznogo Mineral. Obs. (Proc. Sov. Mineral. Soc.)* **1989**, *118*, 90–100. (In Russian)
17. Vanko, D.A.; Bishop, F.C. Occurrence and origin of marialitic scapolite in the Humboldt Lopolith, NW Nevada. *Contrib. Mineral. Petrol.* **1982**, *81*, 277–289. [[CrossRef](#)]
18. Shendrik, R.; Kaneva, E.; Pankratova, V.; Pankrushina, E.; Radomskaya, T.; Gavrilenko, V.; Loginova, P.; Pankratov, V. Intrinsic luminescence and radiation defects in scapolite. *Chem. Phys. Lett.* **2024**, *838*, 141081. [[CrossRef](#)]
19. Rao, Y.; Guo, Q.; Zhang, S.; Liao, L. Comparative Study on Gemmological Characteristics and Luminescence of Colorless and Yellow Scapolites. *Crystals* **2023**, *13*, 462. [[CrossRef](#)]
20. McClure, S.F.; Rossman, G.R.; Shigley, J.E. Tenebrescent scapolite from Afghanistan. *Gems Gemol.* **2005**, *41*, 269.
21. Blumentritt, F.; Fritsch, E. Photochromism and Photochromic Gems: A Review and Some New Data (Part 1). *J. Gemmol.* **2021**, *37*, 780. [[CrossRef](#)]
22. Colinet, P.; Byron, H.; Vuori, S.; Lehtiö, J.P.; Laukkanen, P.; Van Goethem, L.; Lastusaari, M.; Le Bahers, T. The structural origin of the efficient photochromism in natural minerals. *Proc. Natl. Acad. Sci. USA* **2022**, *119*, e2202487119. [[CrossRef](#)] [[PubMed](#)]
23. Sergunenkova, B. Gem scapolite from Turakuloma range (Pamir). *Zap. Vsesoyznogo Mineral. Obs. (Proc. Sov. Mineral. Soc.)* **1989**, *118*, 84–90. (In Russian)
24. Burgner, R.; Scheetz, B.E.; White, W.B. Vibrational structure of the S_2^- luminescence in scapolite. *Phys. Chem. Miner.* **1978**, *2*, 317–324. [[CrossRef](#)]
25. Sidike, A.; Kusachi, I.; Kobayashi, S.; Atobe, K.; Yamashita, N. Photoluminescence spectra of S_2^- center in natural and heat-treated scapolites. *Phys. Chem. Miner.* **2008**, *35*, 137–145. [[CrossRef](#)]
26. Blumentritt, F.; Latouche, C.; Morizet, Y.; Caldes, M.T.; Jobic, S.; Fritsch, E. Unravelling the Origin of the Yellow-Orange Luminescence in Natural and Synthetic Scapolites. *J. Phys. Chem. Lett.* **2020**, *11*, 4591–4596. [[CrossRef](#)]
27. Chukanov, N.V.; Shchepalkina, N.V.; Shendrik, R.Y.; Vidasina, M.F.; Tauson, V.L.; Lipko, S.V.; Varlamov, D.A.; Shcherbakov, V.D.; Sapozhnikov, A.N.; Kasatkin, A.V.; et al. Isomorphism and Mutual Transformations of S-Bearing Components in Feldspathoids with Microporous Structures. *Minerals* **2022**, *12*, 1456. [[CrossRef](#)]
28. Diffraction, O. *CrysAlisPro*; Oxford Diffraction Ltd.: Abingdon, UK, 2009.
29. Petříček, V.; Dušek, M.; Palatinus, L. Crystallographic computing system JANA2006: General features. *Z. Krist. Cryst. Mater.* **2014**, *229*, 345–352. [[CrossRef](#)]
30. Hawthorne, F.C.; Ungaretti, L.; Oberti, R. Site populations in minerals; terminology and presentation of results of crystal-structure refinement. *Can. Mineral.* **1995**, *33*, 907–911.
31. Kresse, G.; Hafner, J. Ab initio molecular dynamics for liquid metals. *Phys. Rev. B* **1993**, *47*, 558. [[CrossRef](#)]
32. HPC-cluster “Akademik V.M. Matrosov”. Irkutsk Supercomputer Center of SB RAS. Available online: <http://hpc.icc.ru> (accessed on 10 September 2024).
33. Kühne, T.D.; Iannuzzi, M.; Del Ben, M.; Rybkin, V.V.; Seewald, P.; Stein, F.; Laino, T.; Khaliullin, R.Z.; Schütt, O.; Schiffmann, F.; et al. CP2K: An electronic structure and molecular dynamics software package-Quickstep: Efficient and accurate electronic structure calculations. *J. Chem. Phys.* **2020**, *152*, 194103. [[CrossRef](#)]
34. Perdew, J.P.; Ruzsinszky, A.; Csonka, G.I.; Vydrov, O.A.; Scuseria, G.E.; Constantin, L.A.; Zhou, X.; Burke, K. Restoring the density-gradient expansion for exchange in solids and surfaces. *Phys. Rev. Lett.* **2008**, *100*, 136406. [[CrossRef](#)] [[PubMed](#)]
35. Neese, F. The ORCA program system. *Wiley Interdiscip. Rev. Comput. Mol. Sci.* **2012**, *2*, 73–78. [[CrossRef](#)]
36. Shendrik, R.; Popov, N.; Myasnikova, A. F-Centers in BaBrI Single Crystal. *IEEE Trans. Nucl. Sci.* **2020**, *67*, 946–951. [[CrossRef](#)]
37. Stephens, P.J.; Devlin, F.J.; Chabalowski, C.F.; Frisch, M.J. Ab initio calculation of vibrational absorption and circular dichroism spectra using density functional force fields. *J. Phys. Chem.* **1994**, *98*, 11623–11627. [[CrossRef](#)]
38. Chivers, T. Ubiquitous trisulphur radical ion S_3^- . *Nature* **1974**, *252*, 32–33. [[CrossRef](#)]
39. Chukanov, N.V.; Vidasina, M.F.; Shendrik, R.Y.; Varlamov, D.A.; Pekov, I.V.; Zubkova, N.V. Nature and Isomorphism of Extra-Framework Components in Cancrinite- and Sodalite-Related Minerals: New Data. *Minerals* **2022**, *12*, 729. [[CrossRef](#)]
40. Hamisi, J.; Etschmann, B.; Tomkins, A.; Pitcairn, I.; Pintér, Z.; Wlodek, A.; Morrissey, L.; Micklethwaite, S.; Trcera, N.; Mills, S.; et al. Complex sulfur speciation in scapolite—implications for the role of scapolite as a redox and fluid chemistry buffer in crustal fluids. *Gondwana Res.* **2023**, *121*, 418–435. [[CrossRef](#)]
41. Jones, J. Al–O and Si–O tetrahedral distances in aluminosilicate framework structures. *Acta Crystallogr. Sect. B Struct. Crystallogr. Cryst. Chem.* **1968**, *24*, 355–358. [[CrossRef](#)]
42. Evans, B.W.; Shaw, D.M.; Haughton, D.R. Scapolite stoichiometry. *Contrib. Mineral. Petrol.* **1969**, *24*, 293–305. [[CrossRef](#)]
43. Chukanov, N.V.; Rastsvetaeva, R.K.; Zubkova, N.V.; Vidasina, M.F.; Pekov, I.V.; Zolotarev, A.A.; Mikhailova, J.A.; Aksenov, S.M. Spectroscopic characterization of extra-framework hydrated proton complexes with the extremely strong hydrogen bonds in microporous silicate minerals. *J. Raman Spectrosc.* **2024**, *55*, 581–597. [[CrossRef](#)]
44. Krivovichev, S. Topology of microporous structures. *Rev. Mineral. Geochem.* **2005**, *57*, 17–68. [[CrossRef](#)]
45. Aksenov, S.; Chukanov, N.; Rastsvetaeva, R.; Pushcharovsky, D.; Burns, P. Crystal chemistry and topology of two and three dimensional zeolites with the modulus based on tetrahedral nets with the apophyllite-type topology. *J. Struct. Chem.* **2024**, in preparation.
46. Krivovichev, S.V. *Structural Crystallography of Inorganic Oxysalts*; OUP Oxford: Oxford, UK, 2009; Volume 22.

47. Blatov, V.A.; Delgado-Friedrichs, O.; O’Keeffe, M.; Proserpio, D.M. Three-periodic nets and tilings: Natural tilings for nets. *Acta Crystallogr. Sect. A Found. Crystallogr.* **2007**, *63*, 418–425. [[CrossRef](#)] [[PubMed](#)]
48. Blatov, V.A.; Shevchenko, A.P.; Proserpio, D.M. Applied topological analysis of crystal structures with the program package ToposPro. *Cryst. Growth Des.* **2014**, *14*, 3576–3586. [[CrossRef](#)]
49. Chen, J.; Natarajan, S.; Thomas, J.M.; Jones, R.H.; Hursthouse, M.B. A Novel Open-Framework Cobalt Phosphate Containing a Tetrahedrally Coordinated Cobalt (ii) Center: $\text{CoPO}_4 \cdot 0.5 \text{C}_2\text{H}_{10}\text{N}_2$. *Angew. Chem. Int. Ed. Engl.* **1994**, *33*, 639–640. [[CrossRef](#)]
50. Ferraris, G.; Belluso, E.; Gula, A.; Soboleva, S.V.; Khomyakov, A.P. The crystal structure of seidite-(Ce), $\text{Na}_4(\text{Ce}, \text{Sr})_2\{\text{Ti}(\text{OH})_2(\text{Si}_8\text{O}_{18})\}(\text{O}, \text{OH}, \text{F})_4 \cdot 5\text{H}_2\text{O}$, a modular microporous titanosilicate of the rhodesite group. *Can. Mineral.* **2003**, *41*, 1183–1192. [[CrossRef](#)]
51. Antao, S.M. Al-Si Order and Chemical Composition Model across Scapolite Solid Solutions with Evidence from Rietveld Structure Refinements. *Minerals* **2024**, *14*, 812. [[CrossRef](#)]
52. Andersson, L. A New Paramagnetic Centre in Scapolite. In Proceedings of the Magnetic Resonance and Related Phenomena: Proceedings of the XXth Congress AMPERE, Tallinn, Estonia, 21–26 August 1978; Springer: Berlin/Heidelberg, Germany, 1979; p. 307.
53. Kaneva, E.; Shendrik, R. Radiation defects and intrinsic luminescence of cancrinite. *J. Lumin.* **2022**, *243*, 118628. [[CrossRef](#)]
54. Colinet, P.; Gheeraert, A.; Curutchet, A.; Le Bahers, T. On the spectroscopic modeling of localized defects in sodalites by TD-DFT. *J. Phys. Chem. C* **2020**, *124*, 8949–8957. [[CrossRef](#)]
55. Vassilikou-Dova, A. An EPR study of scapolite. *Cryst. Res. Technol.* **1991**, *26*, 135–138. [[CrossRef](#)]
56. Viola, C.; Laia, C.A.; Outis, M.; Ferreira, L.F.; Alves, L.C.; Teixeira, M.; Folgosa, F.; Lima, J.C.; Ruivo, A.; Avó, J. Long-lived NIR emission in sulfur-doped zeolites due to the presence of $[\text{S}_3]^{2-}$ clusters. *Mater. Today Chem.* **2023**, *30*, 101514. [[CrossRef](#)]
57. Blažeková, M.; Huraiová, M.; Hurai, V.; Slobodník, M.; Siegfried, P. Two types of scapolite in Evate carbonatite deposit (Mozambique): Implications for magmatic versus metamorphic origins. *Acta Geol. Slovaca* **2019**, *11*, 63–74.
58. Qian, C.; Liu, Y.; Li, X.; Zhu, Y.; Song, H.; Wu, X. Pressure-induced phase transition of CO_3^{2-} -bearing scapolite by in situ X-ray diffraction and vibrational spectroscopy. *Phys. Chem. Miner.* **2023**, *50*, 4. [[CrossRef](#)]
59. Shendrik, R.; Plechov, P.; Smirnov, S. ArDI—The system of mineral vibrational spectroscopy data processing and analysis. *New Data Min.* **2024**, *58*, 26–35. [[CrossRef](#)]

Disclaimer/Publisher’s Note: The statements, opinions and data contained in all publications are solely those of the individual author(s) and contributor(s) and not of MDPI and/or the editor(s). MDPI and/or the editor(s) disclaim responsibility for any injury to people or property resulting from any ideas, methods, instructions or products referred to in the content.